Flow Dynamics and Inclusion Transport in Continuous Casting of Steel

Overview of Significant Findings

This report summarizes some of the many findings obtained from NSF Grant DMI-01-15486, from October, 2001 to October, 2005, which is part of a long-term effort to develop and apply comprehensive models of the continuous casting of steel. Results are reported here for seven interrelated subprojects. After this brief overview of the subprojects, an introduction and background to this project are provided, followed by a detailed description of findings on each subproject. Firstly, models of transient flow using Large Eddy Simulation (LES), which were previously validated with flow measurements, are validated using a rigorous mesh refinement analysis. The validated model is then applied to predict flow, transport, and removal of small inclusion particles, including the inclusion distribution in the solidified steel product for both steady and transient conditions. The model is then applied to larger particles, using a new criterion model for particle capture by a dendritic interface. Of most significance, while more large particles are removed than small ones, the capture rate as defects is still very high. The effect of mold parameters on the flow pattern was investigated, to aid in optimizing flow conditions to avoid other defects, such as level fluctuations and re-entrainment of inclusions from the top surface. Attention was then focused on other removal means. Models of inclusion nucleation, collision, and capture to bubbles were developed, validated, and then applied to predict inclusion removal in both the ladle and the mold. Finally, models of other phenomena important to defect formation were developed and applied to simulate the transport of superheat, thermal-driven flow in top-surface mold flux layers, and the behavior of the interfacial gap and friction.

Introduction

There are great economic, environmental and safety incentives for understanding how to lower the inclusion content of steel. Lowering inclusion-related defects improves steel minimum strength, fatigue life, surface appearance, yield and energy efficiency (from reduced rejects), and thereby increases competitiveness of the steel industry. Consistent lower inclusions levels would allow thinner gage products (with associated weight and energy savings) and could reduce the need for costly and energy-intensive secondary refining steps, such as vacuum arc refining and electroslag remelting. Continuous casting produces 96% of the steel manufactured in the U.S. [1] and is the last, and most important, processing step where inclusions can either be generated or removed. This project investigates inclusion removal during this process through the use of computational models, validated with plant experiments.

Plant observations have found that many serious quality problems, including inclusion entrapment, are directly associated with the flow pattern in the mold.[2] Defects caused by nonoptimal fluid flow are even more important to the nearer-net-shape thin-slab casting processes, which are starting to transform the industry.[3] This is because higher velocities are

required through a smaller inlet nozzle to cast a thin section slab with the same throughput. Thus, design and control of the fluid flow pattern in the continuous casting mold to minimize inclusions is of crucial importance to the steel industry.

The flow pattern in the mold can be controlled by many variables, including the nozzle and mold geometry, submergence depth, steel flow rate, argon injection rate, electromagnetic stirring, and flux layer properties. Many of these parameters are easy and inexpensive to change and yet have a profound influence on flow and corresponding quality. Currently, flow pattern design is done through trial and error, based on qualitative experiments with water models, plant trials, and the plant operator's experience with defects. Identifying an optimal flow pattern is very difficult, because the fundamental relationship between flow pattern and inclusion entrapment has not been quantified. Thus, each casting operation requires its own expensive experiments, and old defects often reappear when changes in the process occur. With so many different operations and new processes to optimize, the industry can no longer afford this approach.

In previous studies, the principal investigators have applied computational models to increase understanding of flow in the continuous casting mold, using both steady-state[4-21] and transient simulations.[22-29] The reliability of these models to predict flow has been demonstrated through comparison with both water models[9-11, 16, 19, 20, 24, 27, 28] and flow measurements in an operating steel caster.[26, 28] The next step is to apply these models to investigate fundamentally, the associated transport and entrapment of inclusion particles and to determine quantitative relationships between flow pattern control parameters (e.g. nozzle geometry) and particle entrapment. The current research is concerned with developing and applying such computations, combined with physical water modeling studies to validate the models and to provide further insight. Finally, plant trials are conducted to further validate the models, and to test proposed improvements. The results of this study should benefit to the steel industry by leading to increased fundamental understanding of inclusion entrapment, and to improvements in design and operating conditions that improve flow pattern in the continuous casting strand and reduce costly defects.

The Process

A schematic of steel processing is depicted in **Fig. 1.1**.[30], with a close-up of the continuous casting mold given in **Fig. 1.2**.

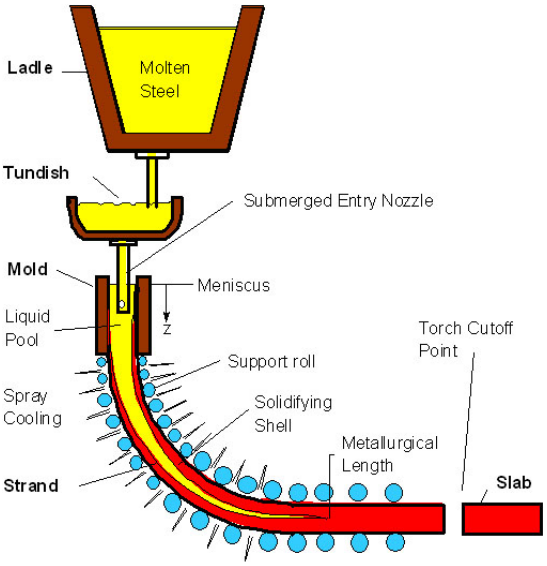

Fig. 1.1. Schematic of Steel Processing including ladle, tundish, and continuous casting

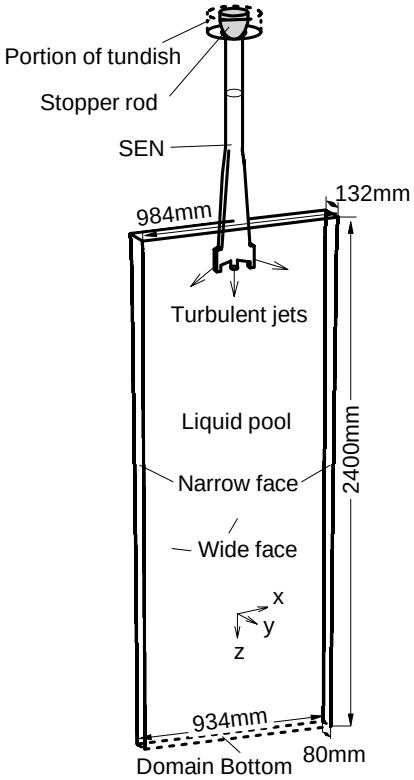

Fig. 1.2. Schematics of the computational domain of the thin-slab steel caster.

Steel is first refined in a ladle to remove as many dissolved impurities and particles as possible. Steel then flows from the ladle through the "tundish," and then exits down through a ceramic Submerged Entry Nozzle (SEN) and into the mold. Here, the steel freezes against the water-cooled copper walls to form a thin solid shell, which is continuously withdrawn from the bottom of the mold at a "casting speed" that matches the flow of the incoming metal. Flow through the SEN is gravity driven by the pressure difference between the liquid levels of the tundish and the mold top free surfaces. The flow rate is controlled (using feedback from a level sensor) to maintain the liquid level in the mold as constant as possible. In one method, a "stopper rod" extends down through the tundish to partially plug the exit. In another method, a "slide gate" blocks off a portion of the SEN pipe section by moving a disk-shaped plate through a horizontal slit across the entire SEN. Such flow adjustment methods allow for independent control of casting speed and metal level, and are essential for stopping the flow of molten steel if the operation must be abruptly terminated. The submerged nozzle protects the molten steel from exposure to air, which helps to avoid reoxidation and inclusion formation. Together with the casting speed, mold geometry, argon gas injection rate, and other parameters, the nozzle geometry also controls the flow pattern created in the mold cavity. This flow pattern in turn controls the entrapment of inclusions and other defects which determine the steel quality.

The Problem

Jets of molten steel exit the nozzle and traverse across the mold cavity to impinge on the solidifying steel shell near the narrow faces. These jets carry bubbles and inclusion particles into the mold cavity. In addition, high speed flow across the top surface may shear droplets of liquid mold slag into the flow, where they may become entrained in the liquid steel.[31] If the flow pattern enables the particles to reach the top surface, they should be harmlessly removed into the liquid slag layer. However, when the flow pattern is detrimental, particles become entrapped in the solidifying steel shell, where they cause serious quality problems and costly rejects. Particle trajectories and removal depend on particle size, which is further complicated by collisions and attachment to bubbles. Particles that become trapped near the meniscus generate surface delamination defects, and may initiate surface cracks. This problem is more likely when there are rapid fluctuations in the level of the top surface. It is also more likely when the meniscus partially freezes to form meniscus "hooks", which entrap particles into the solidifying meniscus before they can enter the liquid slag. Meniscus hooks are more prevalent there is insufficient liquid temperature at the meniscus. The local superheat of the molten steel near the meniscus depends on the flow pattern in the mold, as the jets also transport superheat.

High velocities across the meniscus are detrimental because they cause excessive surface level fluctuations, which enhances particle entrapment. High surface velocities also may entrain some of the molten slag into the steel, where it breaks up into slag inclusions. This is also controlled by the flow pattern in the mold.

Particles which are entrained into the lower recirculation zones can gradually spiral and become trapped in the solidifying front deep inside the product,[15, 32] leading to internal cracks, slivers in the final rolled product, and blisters.[2] One of these defects, known as "pencil pipes",[31] is caused when small argon gas bubbles surrounded by inclusions are caught in the solidifying shell. During rolling, the inclusion clusters elongate to create long slivers in the final product. During subsequent annealing processes, the trapped bubbles expand to create surface blisters.[31] These intermittent defects are particularly costly because they are often not detected until after many subsequent finishing steps.

There is clearly a great incentive to understand how to control the mold flow pattern in order to minimize particle entrapment and the associated quality problems. Furthermore, there are several different phenomena that may contribute to the defects, whose relative importance and mechanisms need to be quantified.

Significant Findings

During the 4 years of this project, significant advances were made on several aspects of this multifaceted research project involving dynamic flow and inclusion transport in the continuous casting mold. They are briefly summarized in the three annual progress reports.[33-35]

The findings are described in more than 45 technical publications and are divided here into the following seven subprojects (with the students that did the work):

1) Transient fluid flow and particle transport (Q. Yuan and L. Zhang)

   1A) Computational issues

1B) Fluid flow and surface level fluctuations

1C) Transport and entrapment of small particles;

1D) Transport and entrapment of large particles

2) Parametric studies (L. Zhang)

3) Nucleation and growth models for alumina inclusions in molten steel (L. Zhang)

4) Inclusion removal via bubbles in the continuous casting mold (J. Aoki and L. Zhang)

5) Flow and heat transfer in a molten flux layer; (B. Zhao)

6) Transient flow and superheat transport in continuous-cast steel slabs (B. Zhao)

7) Interface heat transfer and mold friction (Y. Meng)

1. Transient Fluid Flow and Particle Transport

The first project investigates asymmetric flow in a full model of the process, consisting of both the complete nozzle (including the stopper rod, submerged entry nozzle and ports) and the mold region. Sample results are presented here from two simulations using the LES approach. First, the flow in a full-scale water model was simulated and compared with measurements. Then a simulation of the turbulent flow and inclusion transport in the corresponding full-scale steel caster is performed. The conditions were chosen to match conditions at the AK Mansfield thin slab caster shown in Fig. 1.2 and documented elsewhere [16, 36] where plant measurements were already available (132 x 984mm section, 1 m/min, 59 0C superheat).

1A. Computational Issues in Simulation of Transient Flow in Continuous Casting

Unsteady three-dimensional turbulent flow and heat transport in the liquid pool during continuous casting of steel slabs has been computed using several different computational models, domains, grids, and inlet conditions. Flow patterns in the center plane of three different grids are compared in **Fig. 1.3**. The jet traverses across the domain to impinge on the narrow face, where it turns upward to the top surface and back towards the SEN in a classic double roll flow pattern. The two finest grids are almost identical, showing that grid independence has been achieved. The coarse grid shows an important deviation in jet direction that would have a large adverse effect on secondary calculations, such as particle motion.

To quantify the difference between grids on an equal basis, the velocities computed for each grid were first interpolated onto a 64x128 uniform-spaced grid. Errors for both the time-average and rms velocity were calculated as an average at the center plane y = 0 where the exact solution was estimated using the results from the finest grid (0.8 million cells).

The time average error results are presented in **Fig. 1.4a.** This error increases drastically with increasing grid spacing, which corresponds with decreasing number of cells in the grid. The error between the two finest grids averages only ~0.03m/s, although this represents a 17% difference, relative to the mean velocity in the domain, ~0.18m/s. Coarser grids have errors that are much larger than a glance at the velocity vectors would indicate.

The rms velocity error results are presented in **Fig. 1.4b**. This error also increases greatly with coarsening grid size. These results indicate that the mesh resolution prediction of velocity

fluctuations is accurate within ~0.02m/s or ~17%. The fluctuating velocity component is almost half of the mean velocity component, indicating that turbulence is very strong. Overall, the fine mesh (0.8 million nodes) is believed to produce reasonable results for engineering purposes. A mesh of this refinement was used in subsequent simulations. Further details can be found elsewhere.[37, 38]

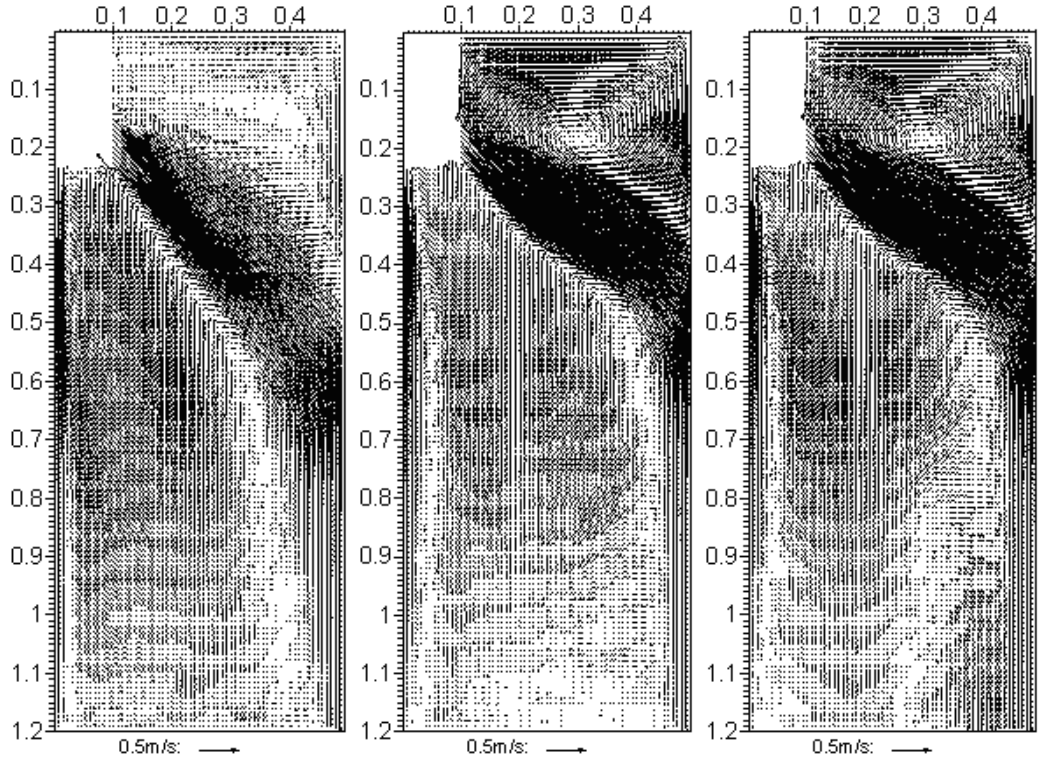

Fig.1.3. Time-averaged velocity fields at the center plane y=0 obtained from LES with $20x10^3$ (left) , $400x10^3$ (middle) and $800x10^3$ (right) computational cells.

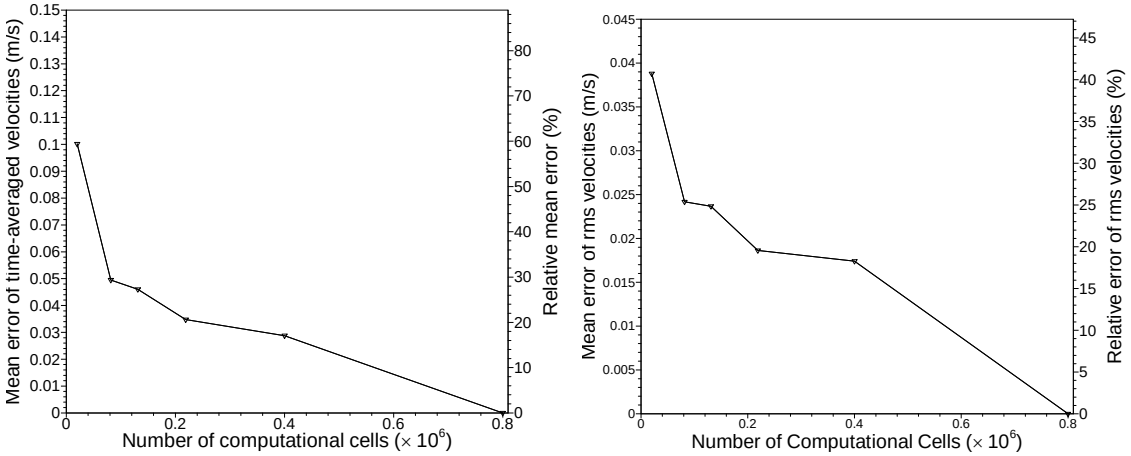

(a) (b)

Fig. 1.4. Effect of grid refinement on error in (a) time-averaged and (b) *rms* velocities.

1B) Flow Model Validation with Measurements

The water model differs from the real steel caster in several respects important to fluid flow. First, the side walls of the water model, which represent the moving solidifying shell, are non-porous and stationary. Further, the water model has a flat bottom with outlet ports to represent the tapering molten pool of a curved casting machine. Figure 1.2 shows the computational domain of the steel caster, which includes these effects. Special source terms were added for both mass and momentum in order to satisfy the conditions on the moving boundaries of the domain, which represent the dendritic solidification front.

Figure 1.5 presents typical instantaneous and time-averaged (over 22 seconds) velocity vector plots at the centerplane of the steel casting machine This particular nozzle geometry features an additional central downward jet entering the mold, in addition to the classic bifurcated nozzle ports sending fluid toward the narrow faces. The turbulent structures in the mold and a slight asymmetry between the two side jets can be seen in this instantaneous plot. The time-averaged plot shows a double-roll flow pattern on each side. Qualitatively similar flow patterns are also seen in the water model simulation.

Figure 1.6 compares LES with the dye injection measurement in the water model. The solid line shows the flow speed along the jet centerline obtained from LES average data. The dark dots present the measured speed. A reasonable agreement is seen between LES and the measurements.

The difference between water models and real steel casting machines is investigated in Figures 1.7 and 1.8, which compare the time-averaged downwards flow velocity (and its rms) of the water model and casting machine along a horizontal line 1000mm below the meniscus and 164mm from the narrow face. The data are time averaged over 48s and 22s for the water model and casting machine respectively. Figure 1.8 shows a bigger spatial variation of the downwards velocity for the water model. It also shows that the steel caster has less upward (ie “reverse”) flow. Two main reasons are suspected to cause this: the tapering and solidification restricts the flow domain, which makes the flow easier to get evenly distributed; and the downwards withdrawing of the shells prevents the flow from having upwards velocities. An asymmetry between the two sides can also be seen for both the water model and casting machine, implying that a low frequency oscillation between the two sides exists and 48 seconds are not enough for the time average.

Figure 1.9 shows the time-variation of the horizontal velocity towards the SEN at the center points between the SEN and the narrow faces on the meniscus, obtained from the steel caster simulation. This figure shows a large transient component, which is observed in water models, but was not observed in half-caster simulations (which assumed symmetrical flow in each half). This suggests that interaction between the two sides of the caster is the cause the large fluctuations. The variations are significant, because the level fluctuations which accompany them are the major cause of defects in the process.

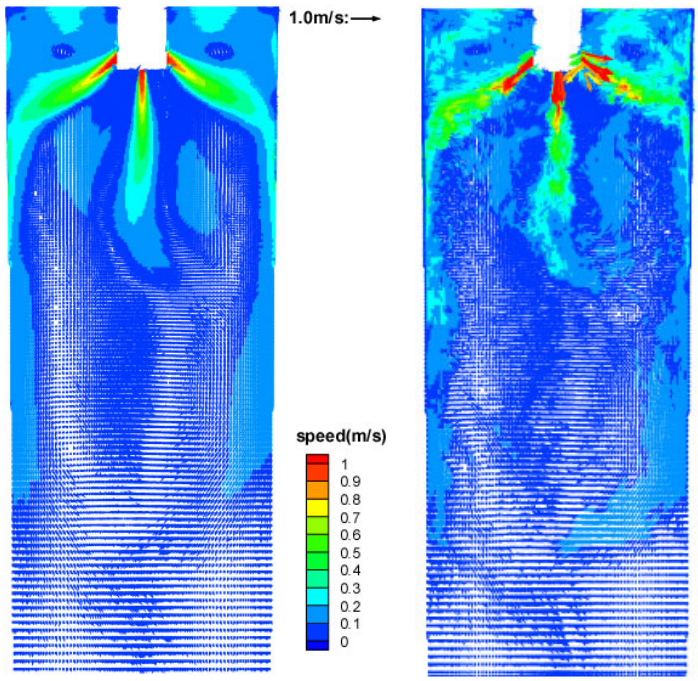

Figure 1.5. Velocity field at the center plane between wide faces (a) time averaged plot, (b) a typical instantaneous plot.

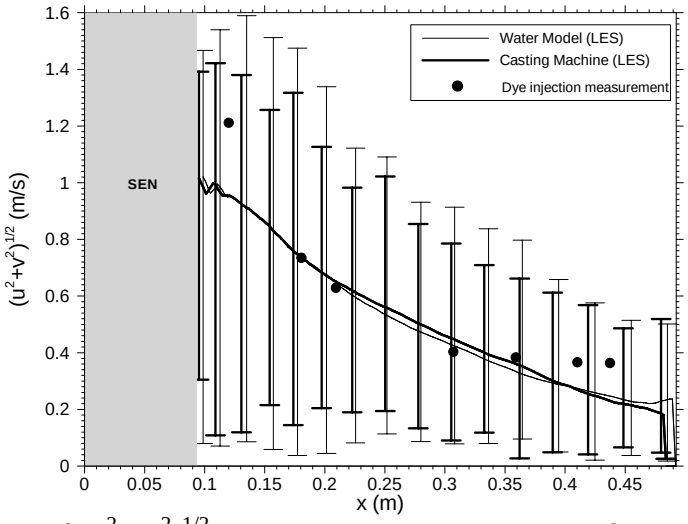

Figure 1.6. Comparison of $(u^2+ v^2)^{1/2}$ along jet centerline, obtained from LES and dye injection measurements (full-scale water model).

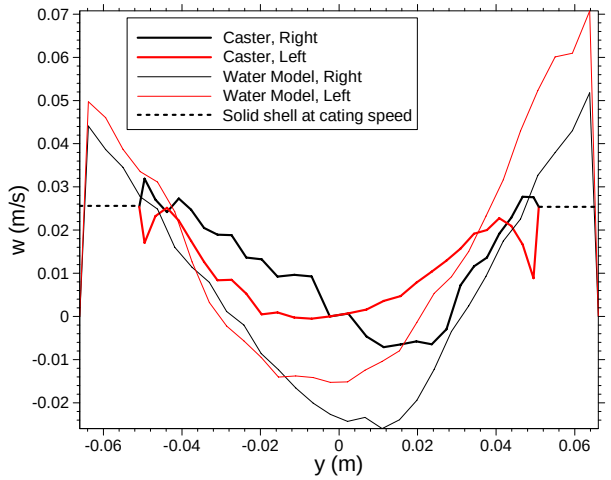

Figure 1.7. Comparison of downwards velocities of the full scale water and casting machine along a horizontal line.

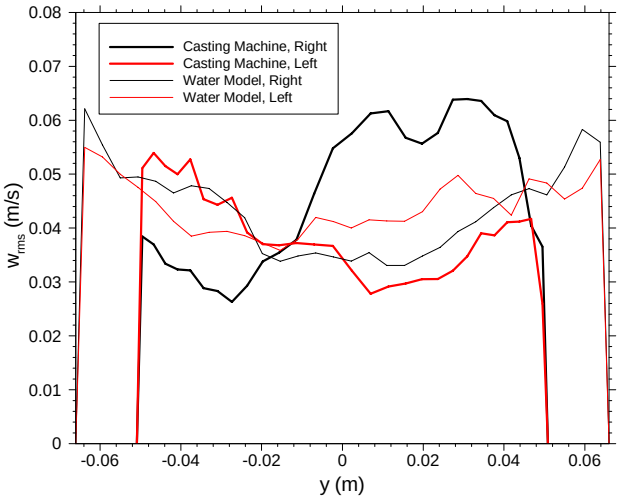

Figure 1.8. Comparison of *rms* of the downwards velocity of the full scale water and casting machine along a horizontal line.

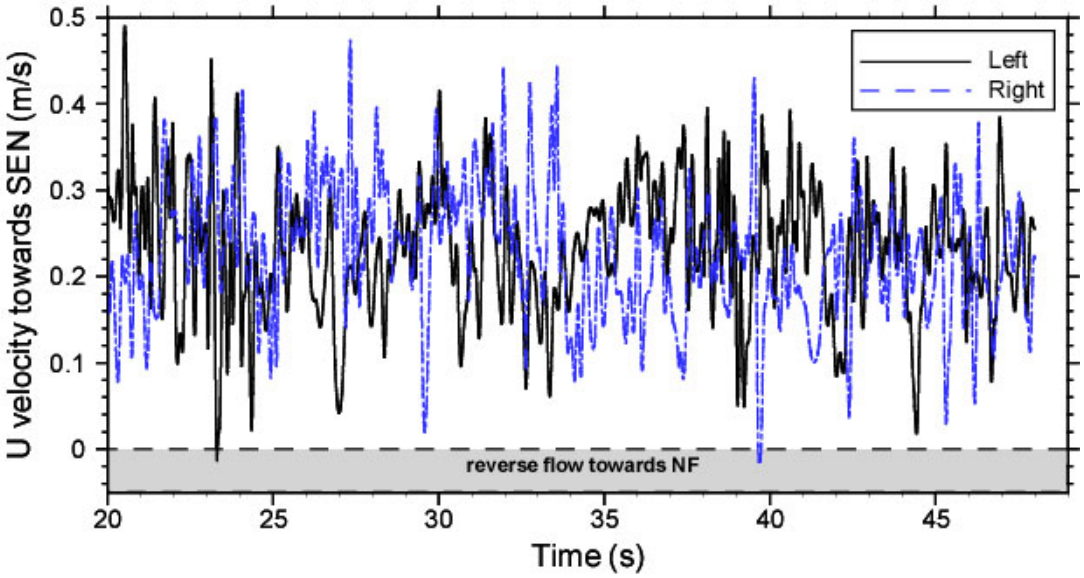

Figure 1.9. Time variation of horizontal velocity towards SEN at the center points of the two sides of the top surface.

Surface Level Fluctuations

Having been validated, the flow model is next applied to investigate related phenomena. Although a critical first step, the flow field is not the primary interest of this project. Defects in the process are generated by the phenomena which accompany the dynamic flow field. These include motion of the top surface level, transport of inclusion particles, and heat transfer. Each of these is discussed in turn:

Figure 1.10 shows an example of the instantaneous variation in surface level predicted from the pressure output from the LES flow model. The level is always higher near the narrow faces, by 4-6mm. This is because the steel momentum up the narrow faces lifts the liquid level there,

displacing some of the molten flux. The flux layer must be thick enough to cover the steel, in order to provide a steady supply of molten flux into the interfacial gap to lubricate the steel. Insufficient flux consumption leads to temperature fluctuations which cause surface cracks and other defects in the solid steel product. Thus, the height of the surface "standing wave" is important to steel quality. The predictions here compare reasonably with industry measurements using nail boards and sheets.

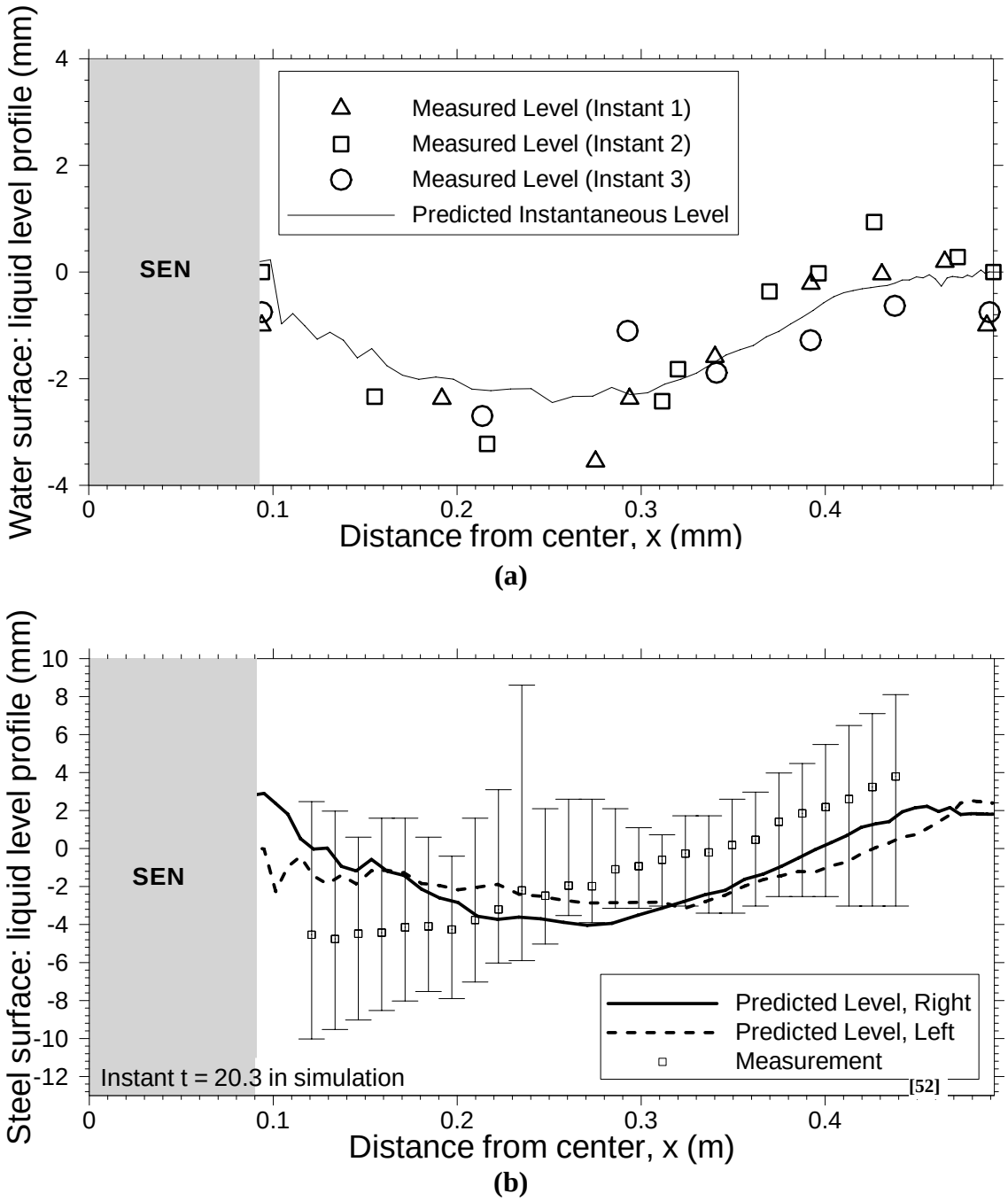

Figure 1.10. Comparison of LES model-predicted and meafsured top surface liquid levels in a) water model and b) steel caster

1C. Transport and Entrapment of Small Particles

Another important consequence of the flow pattern in the mold is the transport of inclusion particles within the molten pool. Inclusions may eventually be removed harmlessly into the top slag layer, or they may become entrapped in the solidifying shell. Fundamental criteria have been developed for the capture of inclusions by a moving dendritic interface through engulfment or entrapment, considering together for the first time: critical interface velocity, particle size, and local cross-flow velocity. Small inclusions (<40 μm) are predicted to become surrounded by the dendrite arms and entrapped with little chance of "particle pushing". Figure 1.11 shows the particle distribution and entrapment locations at three instants for the mold and flow conditions just discussed, for such small inclusions.

Particles are seen to move with the jet and reach the walls 0.6 seconds after injection at 33s. The particles split into two groups by 2 seconds (second frame) and enter the upper and lower rolls. Although the flow and distribution exiting the nozzle is initially almost symmetrical, a significant asymmetry can be seen to develop in the 15 s plot, indicating the important effects of flow asymmetry on particle transport. It is important to note that the inlet velocity distribution was relatively uniform during this time, so the asymmetry in this case is caused solely by chaotic turbulent motion below the mold. The downward motion corresponds to large asymmetry between the velocities at these 2 points, showing that particle motion is dominated by the flow distribution, regardless of particle size. The velocities are seen in Figure 1.12 to fluctuate, indicating that particles injected at other times will show the opposite asymmetry or behave almost the same. These results are important because particles which are transported deeper are more likely to become permanently entrapped in the steel caster.

In this sub-project, Large-Eddy_Simulation models are developed to simulate the transient transport and entrapment of inclusion particles, using a Lagrangian approach based on previous computations of fluid flow in the continuous casting process [39]. This section presents results for particles smaller than the PDAS which can easily enter in between primary dendrite arms and become entrapped with little chance of being pushed away regardless of solidification front velocity [40]. Measurements on the caster of interest here (Fig. 1.2) [36] show that the PDAS is smallest near the top surface (about 50μm) and increases along the casting direction as the solidification rate slows. Thus, this work investigates 10μm and 40μm particles which are predicted to become entrapped instantly upon touching the solidification front, as described in detail elsewhere [41].

Model Validation in a Full-Scale Water Model

The computational model of particle transport was first applied in a full-scale water model, where measurements on particle removal are available [32] The particle fractions removed by the screen at the top surface for the 2,500 and 500 particle groups are presented in Table 1.2, and are also compared with measurements. The average removal fractions for both groups agree with experiments within ±5%. However, the removal fraction varies greatly between groups, especially for the first 10s after particles enter the mold. This is reflected by the standard deviation, which decreases from 5.5% (500 particle groups) and 4.8% (2,500 particle groups) for 0-10s to 2.9% and 1.4% for 10-100s. The standard deviation of the 2,500 particle groups is always lower than that of the 500 particle groups, as expected due to the improvement in statistical confidence with increasing population size. However, the improvement is small for 0-

10s. This suggests that during early times, particle removal is chaotic, because it is dominated by the turbulent eddies of the initial jet. To obtain a more reliable statistical estimate of the mean would require injecting particles during different time intervals. Increasing the number of particles improves the statistics at later times, (e.g. 10-100s) because the standard deviation drops in half. This is because the particles become well dispersed in the liquid pool and random statistics become valid.

Results of Particle Transport and Entrapment in the Thin-Slab Caster

After demonstrating the accuracy of this computational model of particle transport in a standard-slab water model, it then was applied to investigate the transport and capture of small inclusions in the actual thin slab steel caster (Fig. 1.2), in which a trifurcated nozzle is used [16, 36, 41]. The removal and capture history in the strand of the four groups of particles of different sizes and densities are compared in Table 1.3. Particles exiting the nozzle ports could touch the outer nozzle walls, reach the top surface of the liquid pool to be removed, or become entrapped either by touching the solidification front (sides) or exiting the domain bottom. All four different types of particles in Table 1.3 have approximately the same capture and removal histories. Thus, the statistics in Table 1.3 are independent of particle size and density. This is expected because the small buoyancy force relative to drag for these small particles (≤40μm) produces small terminal velocities (≤0.65mm/s) relative to the fluid.

Approximately 8% of the particles that exit the nozzle ports are seen to be removed by the top surface. A further 8% of the particles touched the outside of the nozzle wall while recirculating in the liquid pool and might be removed, depending on the inclusion composition and nozzle properties. Most (90%) of these particles reached the surface within 47s. Most (90%) of the captured particles flowed for less than 72s. The final statistics (Table 1.3) were compiled after all particles exiting the nozzle ports were either removed or captured, which took approximately 220 seconds. Approximately 51% of the particles were captured by the shell in the upper 2.4m of the strand where the shell thickness was less than 25mm (narrow face) or 26mm (wide face). Around 32% of the particles exited the domain from the bottom and would be captured at a deeper (and more interior) position in the solid slab. These results suggest that most (84%) of the small inclusions which enter the mold become entrapped in the final product. Thus, nozzle design and mold operation should focus on controlling flow at the meniscus to avoid the entrainment of new inclusions rather than altering the flow pattern to encourage removal of inclusions entering the mold. This conclusion may differ for large inclusions or if gas bubbles are present.

Inclusion Capture in Solid Steel Slabs after a Sudden Burst: A sudden "burst" of inclusions entering the liquid pool may occur in the continuous casting process during upstream events such as temporary vortexing, release of a nozzle clog or other upset. [42, 43] Knowledge of the inclusion distribution in cast steel slabs caused by such a burst is important for the subsequent inspection and dispositioning of the product. The simulation of a 9s burst of 40,000 inclusions entering the molten steel pool, Fig. 1.14 shows that the 220 seconds needed for all 51% particles to be captured corresponds to a length of around 7m. Most (78.5%) of those particles were captured within 1m above and below the zero-slice. Only a slight asymmetry of the capture positions can be observed from both view angles. This indicates that the flow asymmetries discussed earlier are not significant relative to particle capture. The great asymmetries observed in practice [44] must have been caused by extreme flow asymmetries involving transient events such as a slide gate opening change, or asymmetrical release of a nozzle clog or gas

accumulation. Such events were not considered in this study, but are investigated elsewhere. [23]

Total Oxygen Distribution in Thin Steel Slabs

Total oxygen is often measured to evaluate the content of oxidized inclusions such as alumina in steel slabs. [45] It was calculated based on the computed positions and times of particle capturefor a steady oxygen content of 10ppm (by mass), entering from the nozzle as pure alumina (Al_2O_3) inclusions. The oxygen distribution in a typical cross section through the solidified slab of the steel strand is shown in Fig. 1.15. The dashed line represents the boundaries of the central large cell and is the solidification front at the domain exit (2.4m below meniscus). The highest total oxygen content (about 170ppm) is predicted near the corners, closely followed by intermittent patches on the narrow faces. Intermittent patches with high oxygen concentrations (50-150ppm) are also found in the middle region of the strand (approximately 10-20mm beneath the slab surface). These results indicate that most of the captured particles (69%) are entrapped within the shell approximately 0.4-1.5m below meniscus (corresponding to a shell thickness of 10-20mm).

The finding of increased inclusion capture across the slab width towards the narrow faces agrees with previous measurements [32] and calculations [46] Other measurements find sliver defects concentrated at the surface more towards the wide face centerlines. This is only a slight trend here, owing to impingement from the bottom central port. More severe centerline concentrations would have been predicted if some of the inclusions hitting the top surface were able to continue moving with the flow towards the SEN before being captured in the steel shell at the meniscus. Alternatively, the larger particles which contribute the most to sliver defects have more complex entrapment criteria, such as being pushed along at the solidification front before capture.

Figure 1.16 reveals the oxygen content along the two centerlines shown in Fig. 1.15. Higher inclusion concentrations are found towards the surfaces. Similar variations in total oxygen distribution have been measured in other steel slabs, in which particles were found to concentrate most within 20mm of the slab surface. [47] Small regions with high oxygen content are also distributed sparsely towards the center of the wide faces. This is caused by groups of particles from the center nozzle port. Small patches with low total oxygen close to zero are randomly distributed in the cross section, indicating the effects of turbulent motion of the fluid. Asymmetries can be observed in this symmetrical domain, confirming the influence of fluid instabilities on particle transport and capture. No significant difference is observed between the inside and outside radius, which is consistent with the lack of buoyancy of the small particles considered in this work. In practice, large inclusions are generally of more relevance to quality problems, so future work will focus on developing a capture model for large particles.

1C Conclusions

Lagrangian computations of particle transport during continuous casting of steel slabs were performed in this study. Time-dependent fluid velocity fields obtained from LES were employed in the particle computations. The computational model was applied to simulate the transport and capture of small (10μm and 40μm) inclusions in a thin slab steel caster. The present study confirms the importance of flow transients in affecting the transport and capture of inclusions during continuous casting.

The following conclusions are reached, based on the results of this study:

A comparison of particle removal fractions obtained from 2,500 and 500 particle groups suggests that increasing the number of particles improves the accuracy of removal predictions, for later times (e.g. 10-100s). At least 2500 particles are required to obtain accuracy within ±3%. Particle removal at early times (e.g. ≤10s) is governed by chaotic fluctuations of the flow, which generate variations of ±5%.

The top surface is predicted to remove only 8% of small particles (10μm and 40μm) in the thin slab steel caster. An equal fraction touches the outside of the nozzle walls in the mold. These removal fractions are independent of both particle size and density, owing to the inability of the small, low-buoyancy particles simulated here to deviate significantly from the surrounding fluid flow.

The computation shows that after a 9s sudden burst of particles enter the steel caster, about 4 minutes are needed for all of them to be captured or removed, for the casting conditions assumed here. The captured particles concentrate mainly within a 2-m long section of slab.

With a steady oxygen content of 10ppm from inclusions in the molten steel supplied from the nozzle ports, intermittent patches of high oxygen content (50-150ppm) are found concentrated within 10-20mm beneath the slab surface, especially at the corner, and towards the narrow faces.

Table 1.2. Comparison of fractions of particles removed by the screen in the water model.

		0-10 seconds	**10-100 seconds**
	500 particle groups		
	1	27.2%	23.4%
	2	17.8%	27.2%
	3	26.2%	23.0%
	4	23.8%	23.2%
	5	33.0%	18.2%
	Average	**25.6%**	**23.0%**
	Standard Deviation	5.5%	2.9%
LES	**2500 particle groups**		
	1	27.2%	25.9%
	2	26.8%	27.1%
	3	20.0%	26.5%
	4	23.3%	27.8%
	5	31.8%	24.1%
	6	32.6%	24.9%
	Average	**27.0%**	**26.1%**
	Standard Deviation	4.8%	1.4%
Experiment		**22.3%**	**27.6%**

Table 1.3. Statistics of particle entrapment and removal obtained from thin-slab caster simulation.

		Group 1	Group 2	Group 3	Group 4	Average
Diameter (μm)		40	40	10	10	-
Density (kg/m^3)		5000	2700	5000	2700	-
Fraction of	Captured by shell	51.58%	51.51%	50.79%	51.00%	51.22%
	Captured deeper	32.22%	32.07%	32.77%	32.54%	32.40%
	Removed by top surface	8.03%	8.49%	8.23%	8.20%	8.24%
	Removed by nozzle wall	8.12%	7.83%	8.03%	8.15%	8.03%

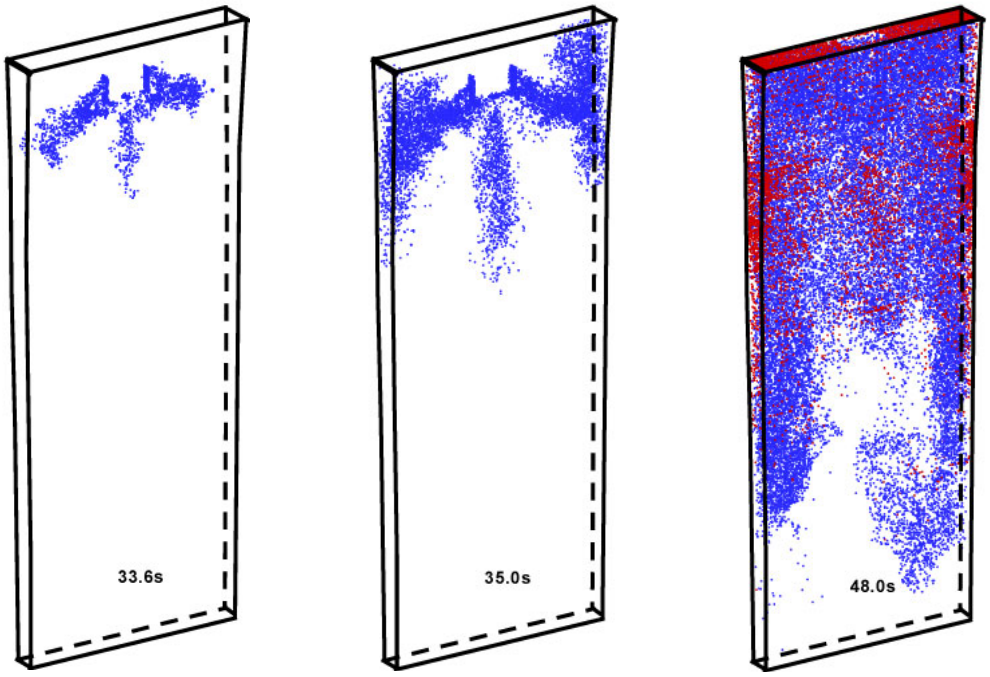

Figure 1.11. Small particle distributions at three instants (blue dots are moving particles; red dots are entrapped particles by solidifying shell).

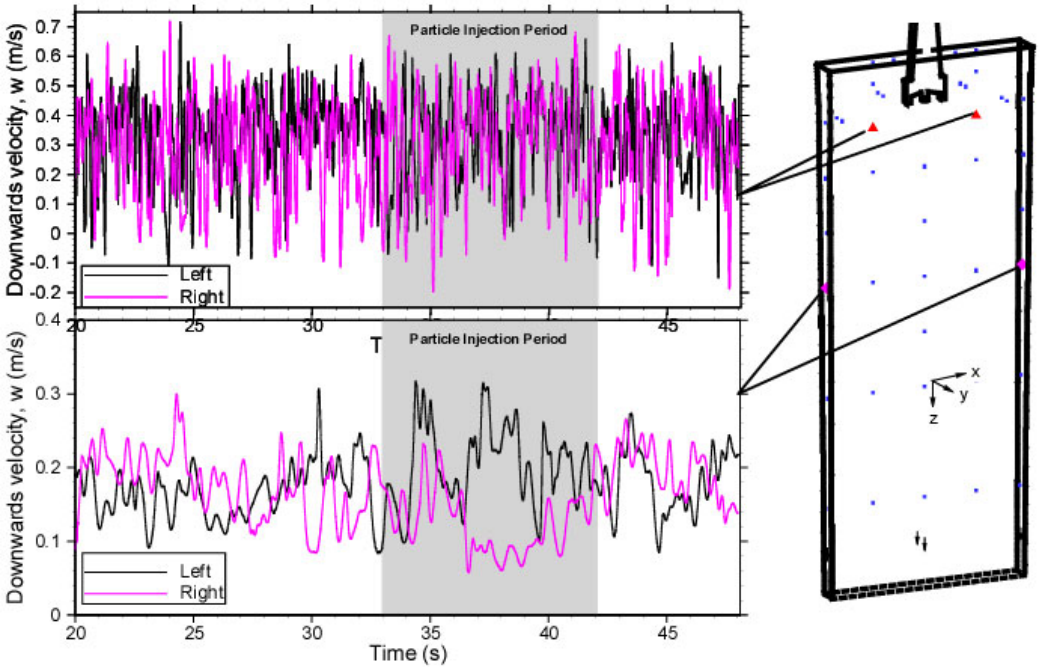

Figure 1.12. Time variations of downwards velocity at two points showing inherent transient asymmetry of the lower rolls.

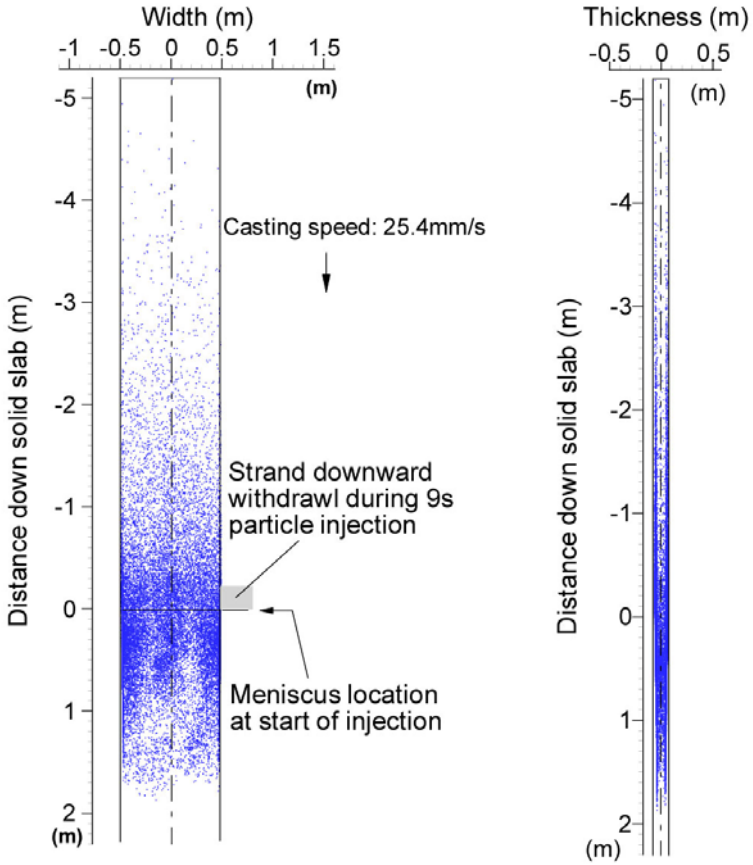

Fig. 1.11. Particle entrapment location for 9s injection: projection onto the wide face (left) and the narrow face (right).

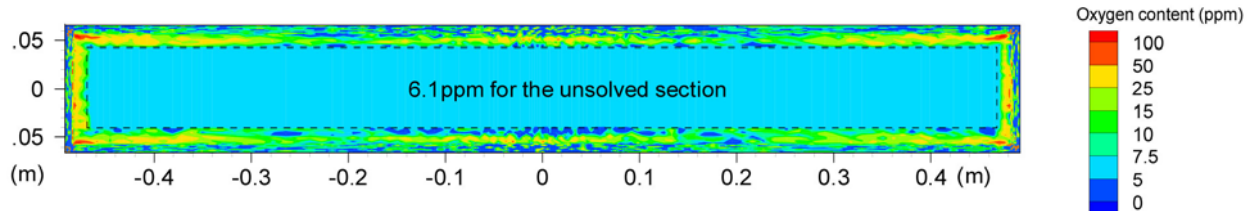

Fig. 1.12. Predicted oxygen concentration averaged in the length direction (10ppm oxygen at nozzle ports).

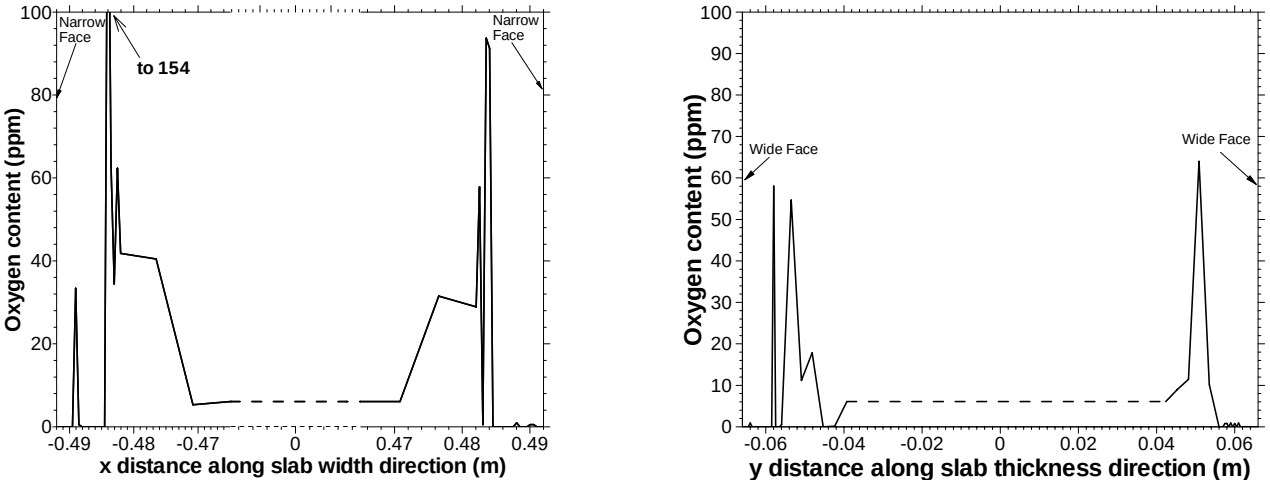

Fig. 1.13. Oxygen content along the centerlines in Fig. 1.15.

1D. Transport and Entrapment of Large Particles

The Large-Eddy_Simulation models were extended to simulate the transient transport and entrapment of large inclusion particles, using the same formation.[39] except for the new capture criterion at the solidification front. This new criterion is described as follows:

1D.1 Modeling of Particle Capture by the Solidification Front: Particles that reach the mushy zone front may be trapped by the solidifying shell or repulsed back into the molten steel flow. The outcome between capture and pushing depends on many phenomena, including the morphology of the solidifying dendrites, the interfacial surface tension governed by the concentration boundary layer of the interfacial active solute (especially the sulfur content), the boundary layer velocity profile, and the particle velocity, size, density and morphology. The flow velocities close to the dendritic interface can be estimated from the LES model during the simulation. However, accurate resolution of the dendrite shape and the concentration boundary layer is computationally prohibitive. To overcome this problem, a novel, but simple criterion for particle pushing and capture has been developed in this work, based on a force balance analysis.

Particles Smaller than the PDAS: Particles smaller than the primary dendrite arm spacing (PDAS), (i.e. $2R_p$<PDAS), can easily flow in between the dendrite arms without major disturbance of their growth. Larger particles cannot do this. If the particle is smaller than the

PDAS, it will be surrounded by the growing dendrites, and it will be captured whenever it reaches the solidification front. The attractive force generated by the surface energy gradient further encourages this to happen. Previous experimental studies [48] in quiescent solidification systems confirm that particles smaller than the PDAS are entrapped, even when the dendrite growth speed is much lower than the critical value for particle pushing. Therefore, a particle smaller than the PDAS is modeled as being captured by the shell whenever it touches a computational boundary representing a mushy zone (solidification) interface.

Particles Larger than the PDAS: Unlike smaller particles, particles larger than the local PDAS cannot fit between the dendrite arms. Figure 1.16 shows a typical dendritic front shape.[49] As depicted in Figure 1.16, a spherical particle of alumina or slag transported to the solidification front contacts the solidifying dendrites through a thin film of liquid steel at the critical distance. If all of the forces acting on the particle are in stable equilibrium, then it will eventually be captured by the solidifying shell as the dendrites grow to surround it. The particle will avoid being captured if the net force acting in the solidification direction push it away from the interface, or if the net force acting across the dendrite front causes it to rotate away. These conditions are checked by considering the balance of the ten different forces which act on the particle in the boundary layer region, including the bulk hydrodynamic forces (lift F_L, pressure gradient, stress gradient, Basset, and added mass forces), transverse drag force F_D, (caused by fluid flow across the dendrite interface), gravity (buoyancy) force F_B, and the forces acting at the interface (Van der Waals interfacial force F_I, lubrication drag force F_{Lub}, and surface energy gradient force F_{Grad}).

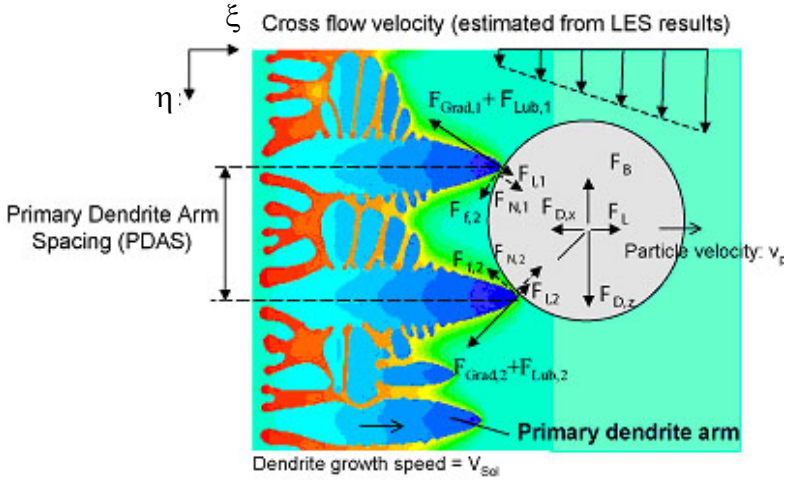

F_D: Drag force; F_{Grad}: Surface energy gradient force; F_I: Van der Waals interfacial force; F_{Lub}: Lubrication drag force; F_L: Lift force; F_B: Buoyancy force; F_N: Reaction force; F_f: Friction force.

Fig.1.16. Illustration of forces acting on a particle in front of solidifying dendrites.

The pressure gradient, stress gradient, Basset, and added mass forces are negligible because they are found to be small (<15% of the buoyancy force) in the bulk region, and are expected to be even smaller in the boundary layer.

The primary dendrite arm spacing needed for this analysis is found from measurements conducted on cast steel, and the dendrite tip radius (r_d) is fitted from corresponding relations.[50] Calculations show that the Van der Waals interfacial force, the lubrication drag force and the surface energy gradient force are only important when the particle is very close to the solidification interface.

Therefore, they can be neglected in the Lagrangian particle transport simulations. These forces are important, however, for evaluating the capture criterion to predict the fate of a particle when it touches a computational boundary representing a mushy zone front.

The results presented previously considered particles smaller than the PDAS (50-140 μm) which can easily enter in between primary dendrite arms and become entrapped with little chance of being pushed away regardless of solidification front velocity.[40] This report focuses on larger particles (100, 250, and 400μm in diameter), which are much more difficult to capture, especially when there is a large transverse velocity.

1D.2 Capture Criterion Model Validation: The particle capture model was tested by applying it in simulations of several different experimental systems where particle capture was measured. Firstly, the model predictions of the critical velocity of the solidification front for the transition from particle pushing to particle capture were compared with measurements of alumina particles in quiescent solidifying liquid steel [51] and zirconia particles in quiescent solidifying aluminum melt.[52] Simulations were then conducted to reproduce the results of the capture or flow of PMMA particles in solidifying water with a tangential (cross) flow across the interfacial front.[53, 54] Both system produced reasonable results, as described in detail elsewhere.[55]

1D.3 Predicted Critical Cross-Flow Velocities in Continuous Steel Caster: Using the validated particle-capture criterion, the critical velocities of the flow relative to the downward moving shell for the capture of slag spheres were computed for typical conditions in a steel caster. The flow was assumed to be vertical (upwards or downwards) across a horizontally-growing solidification front, such as encountered near the narrow face in the continuous casting mold region. The results are shown in Figure 1.17 for the effect of PDAS and a complete range of particle sizes for typical solidification conditions (200μm/s solidification speed and 3.4μm tip radius).

The results illustrate how capture always occurs for particles smaller than the PDAS. Particles larger than the PDAS will be captured if the magnitude of the relative cross-flow velocity between the particle and the solidifying steel shell is smaller than a critical velocity. The magnitude of this critical velocity of the fluid decreases with increasing particle size and decreasing PDAS. Velocity magnitudes higher than the critical value prevent capture, transporting the particle away from the interface before it can get entrapped. This critical velocity depends on the flow direction. Higher critical velocity magnitudes indicate easier capture. Particles are more easily entrapped in downward flow, resulting in higher critical velocity. This is because the upward buoyancy lowers the magnitude of the particle velocity (relative to that for upward flow conditions). The wedge-shaped region of the graph indicates where the capture of large particles is possible. This region becomes narrower as particle size increases, owing to the decreasing ability of the dendrite arms to prevent the rotation of large particles. This region also becomes narrower with decreasing PDAS, again due to easier rotation of particles. The wedge tends towards the terminal velocity of the particle. When the upward terminal velocity equals the downward flow speed (relative to the solidifying shell which is itself moving downwards at the casting speed), then the particle will be stationary relative to the dendrites, so can always be captured (based on results for quiescent flow.[55] With increasing velocity of the solidification front, particle capture becomes easier so the magnitude of the critical cross-flow velocity increases.[55] This effect is small compared with that of particle size, however. This simple, but comprehensive capture model is ready to help predict particle behavior in real castings over a wide range of conditions.

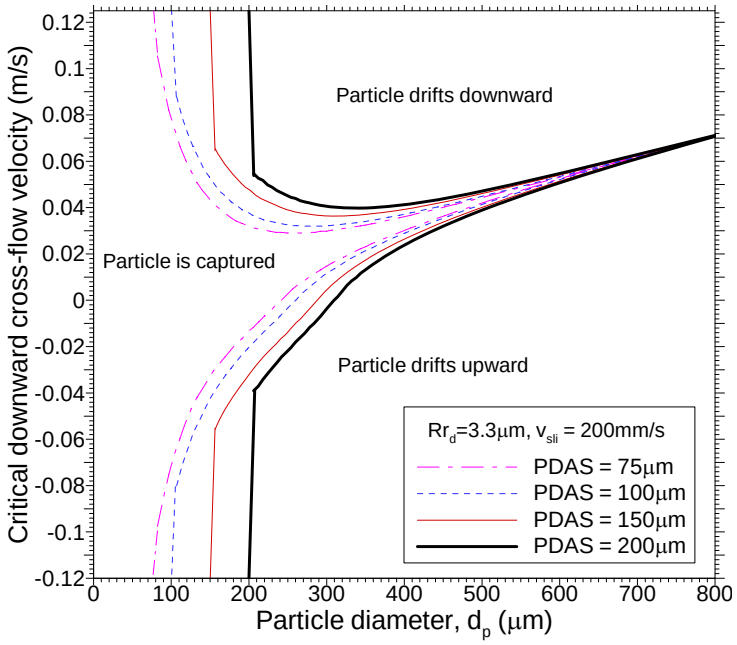

Fig.1.17.Critical downward cross-flow velocities for slag droplets in molten steel.

1D.4 Particle Transport, Removal and Capture in the Thin-Slab Caster: The complete LES model with particle transport and capture criterion was then applied to simulate the transport and capture of three groups of 10,000 inclusions, (2700 kg/m^3 density) and three different sizes (100, 250, and 400μm) in a thin slab steel caster. These inclusions could represent entrained mold slag or alumina particles that entered the mold through the nozzle over a 9s interval.

1D.4.1 Particle Injection through nozzle: After demonstrating the accuracy of this computational model of particle transport in a standard-slab water model, [56], and applying it to investigate the transport and capture of small inclusions in the actual thin slab steel caster[16, 36, 41], it was next applied to investigate the transport, removal and entrapment of large inclusions. The fluid velocities were obtained from LES and conditions are given elsewhere [39].

A typical snapshot of the simulated particle distribution is shown in Figure 1.18 a) (18s after injection of the first particle from the nozzle exit plane). This snapshot is similar to those for small particles presented elsewhere.[56] While they move with the flow, the particles gradually spread apart from the local turbulent eddies. Significant asymmetrical distribution is seen in the lower region. This asymmetry is caused by the unbalanced flow between the two halves of the lower region. The larger downward flow velocities in the right half of Figure 1.18 persisted for more than 50s before the flow became balanced for some time. Then, a similar unbalanced flow pattern occurred again after another 70s. This strong persistent asymmetrical flow deep in the lower recirculation region, was also observed in water models, such as by Gupta and Lahari.[57]

Figure 1.19 shows the removal histories for the 100-400μm particles. More large (400μm) particles were transported to the upper recirculation region and floated to the top surface than small ones (100μm). This is due to two factors. Firstly, the larger particles have larger terminal velocities: the terminal velocities for the 100μm, 250μm and 400μm slag spheres in liquid steel are estimated to be 3.9mm/s, 17.9mm/s and 33.5mm/s respectively, based on equating the drag and buoyancy forces. Secondly, the larger particles are more difficult to capture, as shown in Fig. 1.17.

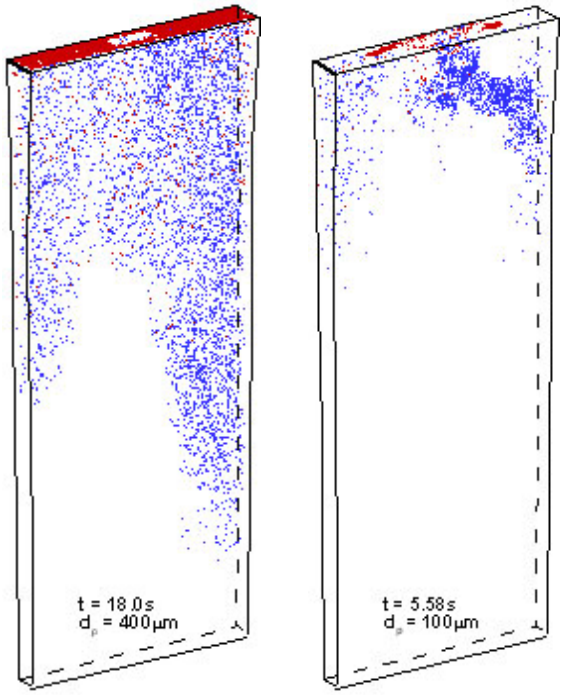

Fig.1.18. Snapshot of distribution of slag particles in the steel caster for a) 400 μm particles entering through the nozzle and b) 100 μm particles entrained at the top surface.

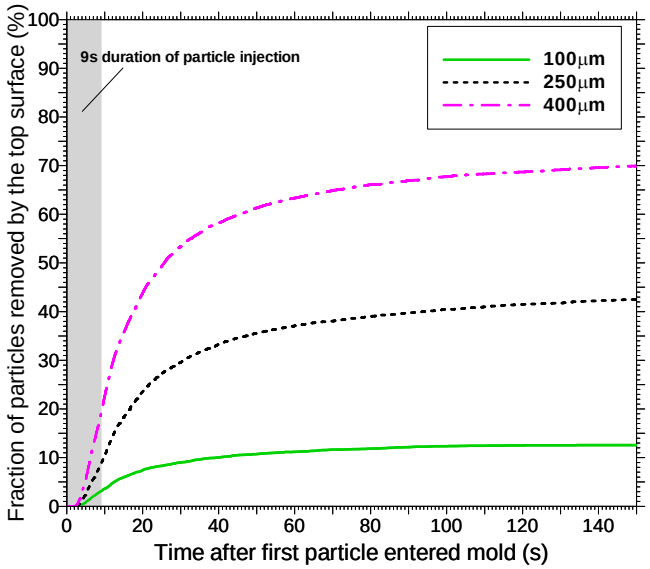

Fig.1.19. Removal and entrapment histories of large particles (>100μm) which entered the mold region from nozzle ports.

Most (~90%) of the particle removal occurred in the first ~50s after the first particle entered the domain. Most (90%) of the captured particles traveled with the flow for less than ~70s. The final removal fractions were 12.6%, 42.5% and 69.9% for the 100, 250 and 400μm particles respectively. These results are consistent with plant observations that particles with sizes ranging from 50μm to 200μm are the main cause of inclusion defects in steel slabs.

The results shown here suggest that very large particles can be effectively removed from the mold region. This is known to be the case for straight-walled casters, and is the reason that many companies have invested in changing their top sections from curved to vertical. Alternatively, the less-buoyant smaller particles always experience small removal fractions. These cause less quality problems owing to their smaller size. Intermediate-sized particles of 100μm - 250μm are large enough to cause severe quality problems, yet are predicted to have high entrapment fractions, even in a vertical caster. Thus, it is important that they are removed from the steel prior to entering the mold. This conclusion may differ if gas bubbles are present, so the effects of gas injection are investigated in a later section.

1D.4.2 Slag entrainment from top surface: During the actual continuous casting process, fingers of the liquid slag layer may be emulsified into the liquid steel from the top surface mold slag layer and broken into spheres by the flow. This is an important alternative source of mold slag inclusions, in addition to those entering the nozzle from upstream.

Figure 7 b) presents a typical snapshot of the distribution of the 100μm particles, 5.6s after entrainment. Again, blue dots denote moving particles and red represents the removed or captured ones. It is seen that immediately after the injection, some of the particles floated to the top surface and were consequently removed. The other particles followed the flow in the upper recirculation region, joined the oblique jet, and then behaved as if they were injected from the nozzle ports. More than 95% of the 400μm particles were safely removed in the first 2s after being entrained into the flow from the top surface slag layer. The final removal fractions exceeded 92% for particles 250μm or larger. However, the removal fraction dropped to 44.6% for the less buoyant 100μm particles. This finding demonstrates that it is very important to control fluid flow in the mold in order to avoid the entrainment of additional mold slag inclusions.

1D.5 Conclusions: Lagrangian computations of particle transport during continuous casting of steel slabs were performed in this study, based on time-dependent fluid velocity fields obtained from LES. For the casting conditions simulated here, the results reveal that:

- Particle entrapment by a solidification front depends on many factors including the particle size and density, transverse fluid velocity, sulfur concentration gradient, solidification front velocity, and primary dendrite arm spacing. A new capture criterion based on a balance of the important forces acting on a particle near a solidification front has been developed, validated with test problems and applied to simulate particle capture in a steel continuous caster.
- Increasing the number of particles improves the accuracy of removal predictions, especially for later times (e.g. 10-100s). At least 2500 particles are required to obtain accuracy within ±3%. Particle removal at short times (e.g. ≤10s) is governed by chaotic fluctuations of the flow, which generate variations of ±5%.
- After a 9s sudden burst of particles enters the steel caster, about 4 minutes are needed for all of them to be captured or removed. The captured particles concentrate mainly within a 2-m long section of slab.
- Most of the inclusions trapped in the steel slab are concentrated within 10-20mm beneath the slab surface, especially at the corner, and towards the narrow faces.

- The safe removal of inclusion particles to the top surface decreases greatly with decreasing particle size. Although the removal fraction of 400 μm particles is 70%, only ~12% of 100 μm particles are removed. Only 8% of small particles (10μm and 40μm) are removed.
- The removal of slag particles entrained from the top surface depends greatly on the particle size. Most (>92%) of the 250μm - 400μm droplets simply return to the slag layer. However, more than half of the 100μm particles are eventually captured, leading to sliver defects.

2. Parametic Studies: Effect of Nozzle Geometry on Inclusion Entrapment

Inclusion removal is affected by many parameters which affect the flow pattern in the mold cavity, including the nozzle and mold geometry, submergence depth, steel flow rate, argon injection rate, electromagnetic stirring, and flux layer properties. Changing nozzle geometry is an easy and inexpensive way to optimize the fluid flow in the mold. Technologies to improve fluid flow and inclusion removal involving the Submergence Entry Nozzle (SEN) include the nozzle port angle, introduction of flow directors that create swirl, multiple outlet ports, throttling plates with oval offset bore, and internal horizontal steps to introduce turbulence. Parametric studies performed using multiphase flow in a water model are reported elsewhere, [35, 58, 59]. The effect of nozzle port angle and the step nozzle technique [60] was investigated using computational modeling, and results are reported here.

2.1 Comparison of Inclusion Removal between Simulation and Industrial Measurements

The distribution of inclusions along the slab thickness measured from microscope observations is shown in Fig. 2.1, which suggests that: 1). Inclusions concentrate more in the 20mm thickness nearest the slab surface; 2). Some slabs have occasional accumulation at the ½ and the ¼ slab thickness from the inner radius; 3). Filters in the tundish are effective at lowering microinclusion levels. Further investigation indicates that this inclusion accumulation is more prevalent in places such as the slab head and tail cast during unsteady conditions. Microscope observation and SEM detection suggest that this inclusion accumulation is mainly induced by the entrapment of dislodged clogged materials from the SEN during the ladle change. Slag inclusions are mainly entrapped at the surface of the slab. The inclusions mass fraction is 66.8ppm in the tundish, 57.7ppm in the 20mm thickness nearest the slab surface, and averaging 51.9ppm in the slab. This suggests that inclusions in the interior of the slab (i.e., except outer 20mm thickness of the slab) is 50.6ppm. The fraction of inclusions removed from tundish to slab is around 22%.

Computed locations of inclusions that attach to the SEN walls and are entrapped at the wide faces of the slab and inclusion measurement are shown in Table 2.2. The calculation suggests that around 12% of the inclusions leaving the tundish stick to the SEN walls (removed by clogging). The buildup is roughly uniform on the nozzle walls, with increased tendency towards buildup on the SEN bottom due to impact from the flowing jet. This is consistent with observations of nozzle clogging where local reoxidation or chemical interaction were not the cause.

For inclusions smaller than 50 μm entering the mold, only 7% are safely removed by the top surface (6% from tundish to slab), independent of inclusion size. A larger fraction of inclusions bigger than 50 μm are removed. The majority of inclusions leaving the tundish (more than 60%) are captured within 30mm of the surface, which represents the top 2.55m of the caster. Fig. 2.1 also shows that inclusions accumulate peaks are at 12-14mm below the surface of the slab. This

agrees only qualitatively with measurements in Fig. 2.1. A disproportionately large fraction of these (15-16%) are captured in the narrow face, despite its smaller surface area, owing to the jet impingement against its inner solidification front. Inclusions exiting the domain are entrapped somewhere deeper in the interior than 30mm shell thickness.

If the entrapment criterion is the same for small and large inclusions, then their entrapment behavior is similar. (This assumption will be refined in future work). Only 3-12% of the inclusions entering the mold are predicted to be removed by the top surface (2.6-11% from tundish to slab). Adding 12% sticking to the SEN walls as clogged material, the simulated inclusion removal from tundish to slab is 18-23%, which agrees with the measurement of 22%.

Although this relatively simple model still needs to be validated rigorously with the more refined LES model, this aproximate agreement is encouraging. Both experiments and models suggest that the removal rate of small inclusions in the mold is quite small.

2.2 Effect of SEN Port Angle and Steps on Flow and Inclusion Removal

Due to the sharp decrease of the bore diameter at the steps, the fluid flow is accelerated at these locations in the Step SEN. This acceleration helps to diminish the non-uniform velocities generated by the slide gate, as shown in Fig. 2.2 (center). Without steps, the uneven flow passing the slide gate eventually generates a swirl at the bottom of the nozzle and in the jets entering the mold. This swirl is diminished in the Step SEN. Jet characteristics for nozzles with outports angle of 15^o down, 0^o horizontal, 15^o up, and Steps are compared in Table 2.3. The 15^o down nozzle with two steps has the smallest turbulent energy and dissipation rate, which means the jet entering the mold has the weakest turbulence. The jet angle is only 18^o down for the Step SEN (15^o down), compared with 29^o without steps (15^o down), and 18^o for Zero degree angle nozzle without Steps. The large jet angle causes a deep impingement point, which lessens inclusion removal to the top surface. One problem of the Step SEN is its large back flow zone fraction, 30%, compared with all three conventional nozzles in Table 2.3. The larger back-flow zone will bring more inclusions back to the outport region of SEN, possibly inducing clogging there.

All four nozzles investigated have a classic double roll flow pattern for these conditions of deep 300mm submergence and no gas injection. The upper loop reaches the meniscus and may increase the surface height near the narrow face. The lower loop takes steel downwards into the liquid core where it eventually flows back towards the meniscus in the strand center. However, the impingement point on the narrow face and the jet penetration depth is different. Without steps, the penetration depth is deeper than with steps. The steepest nozzle angle naturally produces the deepest penetration depth. Results indicates that annular steps in the SEN decreases the penetration depth. The eye of the lower loop with steps is higher than without.

The fraction of inclusions transported to different destinations are shown in Table 2.4. For the current domain length 2.55m, and the current casting speed 1.2m/min (0.02m/s), the shell thickness at the open bottom of the domain is around 30mm, based on solidification model results [61]. Of the 50 μm inclusions entering the mold, 31.4% are predicted to be entrapped in the central region of the slab (30-125mm thick) using the non-step 15^o down nozzle. This number decreases to 15.7% for the stepped 15^o down nozzle, 17.1% for the zero angle nozzle, and 29.4% for the 15o up nozzle.

For the down 15 ^{o} angle nozzle, only 3% of the inclusions are removed to the top surface, but this number increases to 7% with two annular steps. The step nozzle is predicted to have slightly more inclusion removal to the top surface of the mold, perhaps by eliminating swirls at SEN outports and in the mold, and deceasing the impingement depth of the jet in the mold. Table 2.4 also shows that a disproportionate number of inclusions are entrapped by the narrow faces (18%) compared with the wide faces (50-60%). From the average residence time of inclusions prior to entrapment, the positions of inclusion accumulation peaks near the surfaces of the slab can be calculated. The results indicate that inclusions accumulate at 12-14mm below wide surfaces, and 9-10mm below the narrow surfaces. Because the inclusion removal rates are so small for all nozzles, it is more important to choose nozzle designs that produce optimal conditions at the meniscus to avoid slag entrainment, level fluctuations, and other problems.

2.3 Parametric Study: Flow Optimization Using Water Models

Parametric studies with the water models and plant measurements reveal:

- Three kinds of fluid flow pattern are observed in the SEN: bubbly flow, annular flow, and an intermediate critical flow structure. The annular flow structure induces detrimental asymmetrical flow in the mold. Moreover, its higher resistance to flow makes switching between flow structures prone to level fluctuations, which is even more detrimental.

- The SEN flow structure depends on the liquid flow rate, the gas flow rate, and the liquid height in the tundish. The gas flow rate should be adjusted with changes in the casting speed in order to maintain stable bubbly flow.

- Two main flow patterns are observed in the mold: single roll and double roll. The single roll flow pattern is generated by large gas injection, small SEN submergence depth and low casting speed. To maintain a stable double-roll flow pattern, which is often optimal, the argon should be kept safely below a critical level.

- The chosen optimal nozzle had 45mm inner bore diameter, downwards 15^{o}port angle, and 0.44 port-to-bore area ratio, and with recess bottom shape.

- Mass balances of inclusions in the steel slag from slag and slab measurements shows that around 22% inclusions are removed from the steel into the mold slag. However, entrainment of the mold slag itself is a critical problem. Inclusions in the steel increase two-fold during ladle changes. Slabs cast during the start and end of a sequence have the most inclusions.

2.4 Conclusions

Measurement indicates that trapped inclusions concentrate mostly within 20mm of the slab surface. Some slabs have occasional concentration at the ¼ slab thickness from the inner radius, mainly induced by the entrapment of released clogged materials from the SEN during ladle exchanges. In the continuous caster, around 12% of inclusions leaving the tundish are removed by sticking to the SEN walls, and only 3-11% are predicted to be removed to the top slag of the mold. This roughly matches the measured total inclusion removal fraction to the top surface of 22%. The majority of simulated inclusions entering the mold (60%) are captured within 30mm of the surface of the slab, which represents the top 2.55m of the caster. Simulation indicates that

inclusion accumulation peaks are at 12-14 mm below the surface of the wide face, which agrees well with the measurement. The removal rates do not vary much with nozzle geometry.

Table 2.2. Fractions of inclusions entrapped at different locations after leaving tundish

Simulation	Size	SEN walls	Top slag of mold	Slab		
				Narrow face	Wide face	Interior
				0-30mm	0-30mm	30-125mm
	50μm	**12%**	**2.6-6.9%**	15-16%	40-43%	15-28%
	225μm	**12%**	**11%**			
Measurement	All	**22%** (decrease from tundish to slab)				

Table 2.3 Jet characteristics of SEN with different outport angles or SEN steps

SEN Outport angle	Down 15	Down 15	Zero	Up 15
With steps or not	No	Two Steps	No	No
Weight average x velocity (m/s)	0.80	0.96	0.87	0.86
Weight average y velocity (m/s)	-0.0351	0.012	0.0018	-0.007
Weight average z velocity (m/s)	0.45	0.32	0.14	0.28
Weight average turbulent energy (m^2/s^2)	0.27	0.20	0.32	0.31
Weight average turbulent energy dissipation rate (m^2/s^3)	6.41	5.27	10.47	8.88
Vertical jet angle (^{o})	29.29	18.23	9.10	17.76
Horizontal jet angle (^{o})	-2.52	0.72	0.12	-0.47
Jet speed (m/s)	0.92	1.01	0.89	0.90
Back-flow zone fraction (%)	15.31	29.38	26.15	20.73
With swirl or not at Outports	With	No	With	With

Table 2.4 Inclusion fractions to different destinations, and average residence times before entrapment

	Fractions to different destinations (%)						Average residence times (s)				
	Top	Wide1	Wide2	Narrow	Bottom		Top	Wide1	Wide2	Narrow	Bottom
Down15^o	2.9	20.5	27.5	17.6	31.4		23.7	23.9	22.5	13.5	25.9
Down15^o (Steps)	6.9	28.9	30.3	18.2	15.7		11.1	23.6	26.1	13.0	49.1
Zero	5.1	23.5	35.8	18.4	17.1		22.7	26.7	20.4	14.8	31.7
Up15^o	2.8	20.4	28.0	19.3	29.4		21.7	41.7	33.3	19.5	54.5

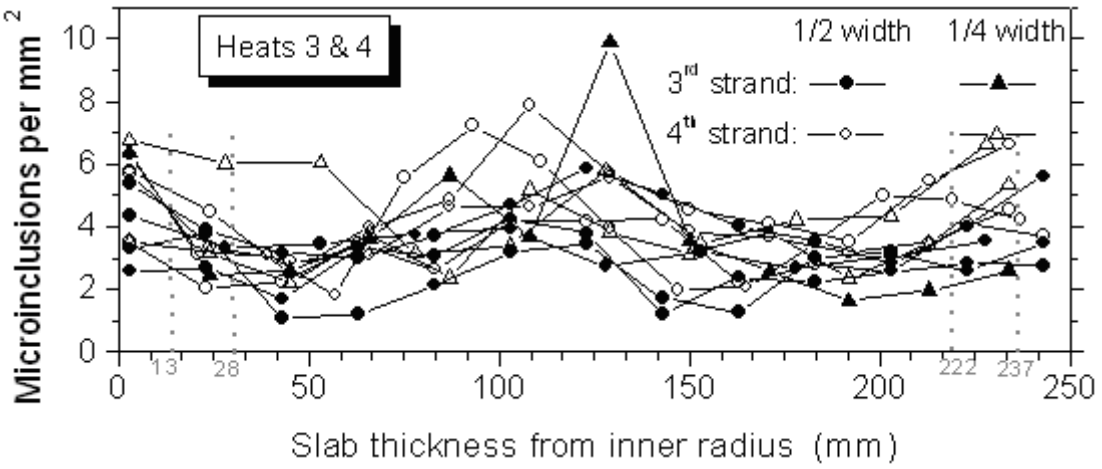

Fig.2.1 Inclusions distribution (<50μm) along the slab thickness with (strand 3) and without (strand 4) tundish filters

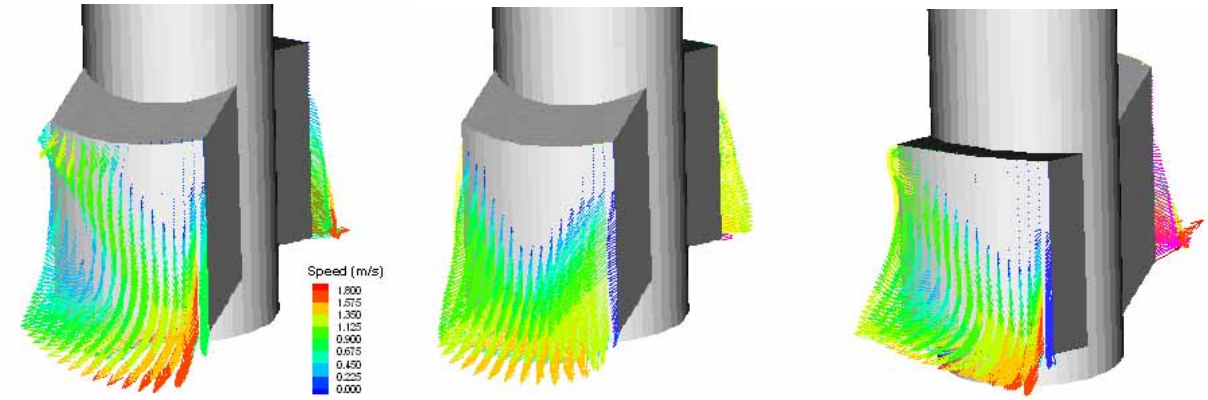

Fig. 2.2 Flow pattern at outports of 15° down angle without steps (left), 15° down angle with steps (middle), 15° up angle without steps (right)

3. Nucleation and Growth Models for Inclusions in Molten Steel

Inclusion size and number distribution is greatly affected by collisions with other inclusions, and varies continuously during processing, so tracking the evolving size distribution during the flow process is desirable. A model has been developed to predict inclusion size distribution evolution and applied to a ladle [62-64]. In addition to being a simple test system for model development, inclusion removal from ladles is of critical importance in removing inclusions from the final product, as the previous results have shown that it is very difficult to remove many of the inclusions that enter the mold.

This size-grouping model of inclusion nucleation and growth by diffusion, Brownian collisions, and turbulent collisions was applied to simulate inclusion evolution in a typical ladle [64], where measurements were available. The vessel was a 50 tonne ladle of low-carbon steel refined in an ASEA-SKF furnace.[65] The total oxygen before adding aluminum is around 300 ppm and the final free oxygen is about 3 ppm, which corresponds to a 46kg aluminum addition. The ladle had 2.3m diameter and 1.7m depth.

3A. Nucelation & Collision Model Findings

Starting with rapid supersaturation with Al_2O_3 "pseudo-molecules", homogeneous nucleation is very fast, occurring mainly between 1μs and 10μs. The stable inclusion nuclei are predicted to be only about 10-20 Å in diameter. The growth of inclusions smaller than 1μm in radii is mainly controlled by diffusion of pseudo-molecules and Brownian collision, and inclusions in this range tend to be spherical. The growth of inclusions larger than 2μm in radii is mainly controlled by turbulent collisions, and inclusions in this range tend to form clusters which retain minimum feature sizes of 1~2μm.

Assuming that all inclusions with radii larger than 36μm are instantly removed to the top slag, the computed inclusion size distribution evolves greatly during reefing. The distribution can reach 0.1~1μm at 6s and 0.1~36μm at 100s, which agrees roughly with the industrial measurements [66, 67] After 720 seconds, total oxygen in the steel decreases to around 20 ppm, which agrees with other measurements. [65]

3B. Ladle Mixing Times

Aluminum is added into molten steel from solid aluminum to melt and dissolve into free aluminum atoms. Once the solid aluminum is dissolved, the aluminum atoms are available to react with the free oxygen in the molten steel to generate alumina inclusions. The calculated nucleation time is in the order of 1μs, which is very fast compared with the mixing of aluminum atoms in the molten steel. Figure 3.1 shows the aluminum dispersion in an argon stirred ladle of molten steel, which indicates that the mixing process is much slower, roughly 108 times slower than the nucleation process. The mixing time is defined as the time at which the mass fraction reaches 95% of the infinite average fraction. The calculated mixing times vary greatly at different points in the ladle, as shown in Fig. 3.2. Within this uncertainty, the computations in figure 3.2 agree with previous measurements [68]. Increasing stirring power naturally decreases the mixing time. Inclusion trajectories in this argon-stirred ladle also shown in Fig. 3.3, which indicates a long moving path length before inclusions reach the top surface to be removed.

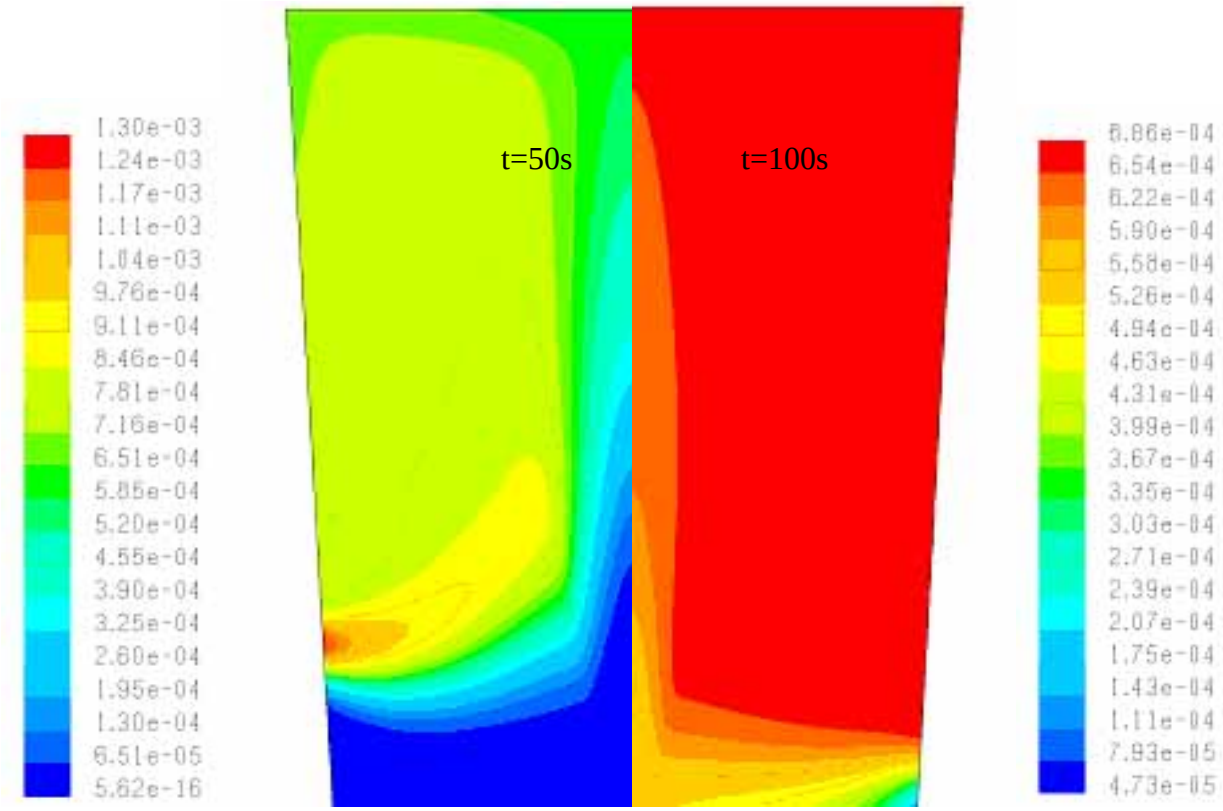

Fig.3.1 Aluminum mass fraction distribution in ladle at different time

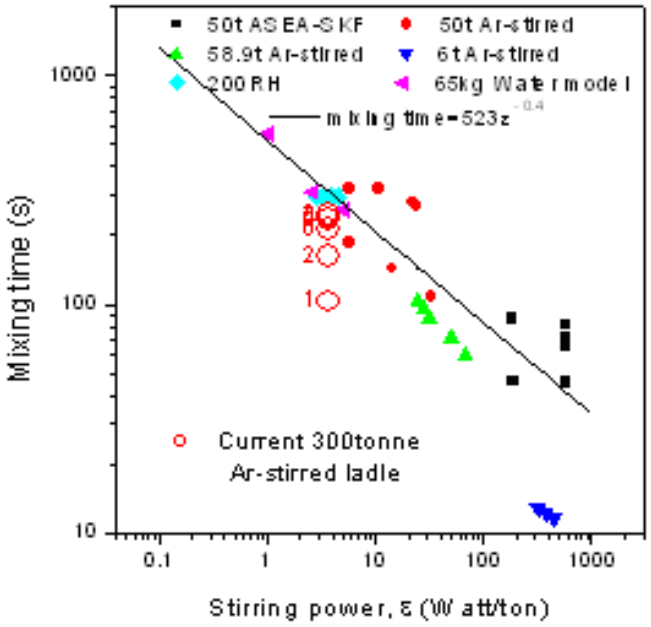

Fig.3.2 Mixing time deceasing stirring power

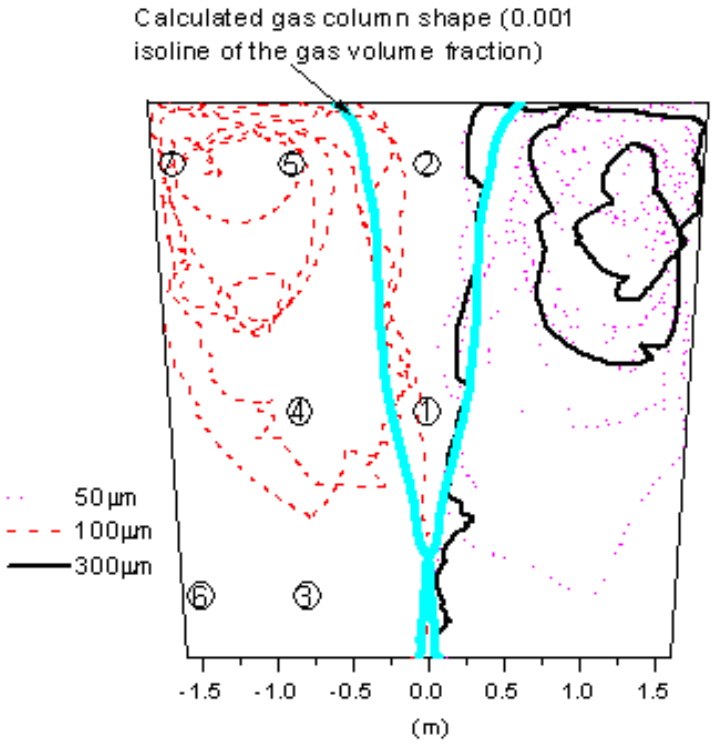

Fig.3.3 Inclusion trajectories in argon stirred ladle

In addition to providing needed input conditions for the mold inclusion calculations, the deoxidation model also reveals important insights into optimal steel refining practice. The effect of stirring power on the oxygen removal rate constant in different steel refining vessels was computed and compared with other measurements [69, 70]. Excessive stirring is detrimental as the upward circulation of steel onto the slag layer may expose an "eye" region of the steel surface to reoxidation and the lining may be seriously eroded. The calculated effect of stirring power on inclusion size distribution indicates that increasing stirring power generates more large inclusions in the bulk. If these inclusions can be removed into the slag, this improves cleanliness. This is very bad for steel cleanliness, however, if the stirring power is high at the end of refining, when the new large inclusions have no time to be removed. Therefore, the recommended practice is to first stir vigorously, to encourage the collision of small inclusions into large ones, followed by a "final stir" that slowly recirculates the steel to facilitate their removal into the slag while minimizing the generation of more large inclusions via collisions.

4. Inclusion Removal by Bubble Flotation in Continuous Casting Mold

Fundamentally-based computational models are developed to quantify the removal of inclusions by bubbles during the continuous casting of steel. First, the attachment probability of inclusions on a bubble surface is investigated based on fundamental fluid flow simulations, incorporating the turbulent inclusion trajectory and sliding time of each individual inclusion along the bubble surface as a function of particle and bubble size. Then, the turbulent fluid flow in a typical continuous casting mold, trajectories of bubbles and their path length in the mold are calculated. The change in inclusion distribution due to removal by bubble transport in the mold is then calculated based on the computed attachment probability of inclusion on each bubble and the

computed path length of the bubbles. In addition to quantifying inclusion removal for many different cases, the results are important to estimate the significance of different inclusion removal mechanisms.

4.1 Inclusion-Bubble Interactions in Molten Steel: In molten steel, bubbles smaller than 3mm tend to be spherical, 3-10mm bubbles are spheroidal, and bubbles larger than 10mm are spherical–cap shaped. The bubble size depends mainly on the gas flow rate, injection method and stirring power in the molten steel. The average equivalent size of bubbles is estimated to be ~5mm in the CC mold investigated in this work.

The attachment process of an inclusion to a gas bubble in the molten steel proceeds through the following steps: the inclusion approaches the gas bubble, and collides if it gets close enough. If the thin film of liquid between the particle and the bubble decreases to less than a critical thickness, it will suddenly rupture causing the inclusion to attach permanently to the surface of the bubble during the collision. Alternatively, if it slides along the surface of the bubble for a long enough time, the thin film can drain away and rupture, again leading to inclusion attachment. Otherwise, the inclusion will move away and detach from the bubble.

The attachment probability, is the fraction of particles in the column traversed by the path of the bubble that are captured onto the bubble surface. The attachment probability of different-sized inclusions (d_P=5, 10, 20, 35, 50, 70,100μm) to different-sized bubbles (1, 2, 4, 6, 10mm diameter) are shown in Figure 4.1, without considering the stochastic effect. This figure indicates that smaller bubbles and larger inclusions have larger attachment probabilities. Specifically, 1mm bubbles can have inclusion attachment probability as high as 30%, while the inclusion attachment probability to >5mm bubbles is less than 1%. A minimum-efficiency bubble size exists of ~7mm. Smaller bubbles attach more inclusions, owing to their higher surface area to volume ratio. Large bubbles are more efficient because of their spherical-cap shape.

To enable computation of attachment rates for a continuous size distribution of inclusions and bubbles, regression was performed on these calculated attachment probabilities, resulting in Eq.[14], which is included in Fig.4.1.

$$P = Ad_p^B \qquad [14]$$

where A and B are

$$A = 0.268 - 0.0737d_B + 0.0615d_B^2 \qquad [15]$$

$$B = 1.077d_B^{-0.334} \qquad [16]$$

where d_B is in mm, d_p is in μm.

The simulation results indicate that the stochastic effect increases the attachment of inclusions to the bubble surface by around 1.4 times, relative to these predictions of the non-Stochastic model.

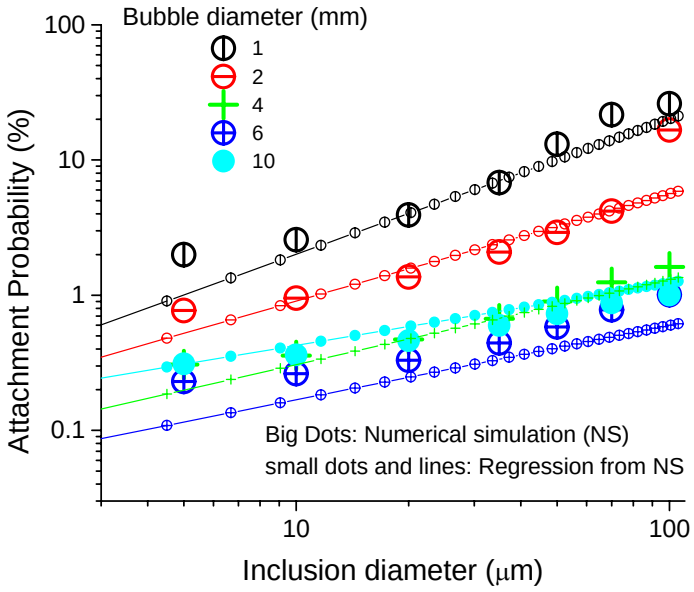

Fig.4.1 The calculated and regressed attachment probability of inclusions to bubbles

4.2 Fluid Flow and Bubble Motion in the Continuous Casting Strand: The three-dimensional single phase steady turbulent fluid flow in the SEN and CC strand produced a calculated weighted average turbulent energy and its dissipation rate at the SEN outport are 0.20 m^2/s^3 and 5.27 m^2/s^3 respectively. The calculated velocity vector distribution on the center face of the half strand indicates a double roll flow pattern. The calculated weighted average turbulent energy and its dissipation rate in the CC strand is 1.65×10^{-3} m^2/s^2 and 4.22×10^{-3} m^2/s^2 respectively. The results indicate that smaller bubbles penetrate and circulate more deeply than the larger ones. Bubbles larger than 1mm mainly move in the upper roll. 0.2mm bubbles can move with paths as long as 6.65m for a time of 71.5s before they escape from the top or become entrapped through the bottom, while 0.5mm bubbles move 3.34m during 21.62s, 1mm bubbles move 1.67m during 9.2s, and 5mm bubbles move 0.59m during 0.59s. The mean of the path length (L_B) and the residence time (t_B) of the bubbles depend on the bubble size as follows:

$$L_B = 9.683\exp\left(-\frac{1000d_B}{0.418}\right) + 0.595 \qquad [17]$$

$$t_B = 195.6\exp\left(-\frac{1000d_B}{0.149}\right) + 23.65\exp\left(-\frac{1000d_B}{0.139}\right) + 2.409\exp\left(-\frac{1000d_B}{8.959}\right) \qquad [18]$$

where the path length L_B and bubble size d_B are in m, and the residence time t_B is in s.

4.3 Inclusion Removal by Bubbles in the CC Strand:

The inclusion size distributions measured in the tundish above the outlets and in the CC slab are shown in Figure 4.2 together with the calculated size distributions after inclusion removal by bubble flotation for several different bubble sizes. The corresponding inclusion removal

fractions are shown in the adjacent frame. If the bubbles were larger than 5mm, less than 10% of the inclusions can be removed by bubble flotation at the gas flow rate of 15 Nl/min. This corresponds to a 3ppm decrease in total oxygen. Smaller bubbles appear to cause more inclusion removal for the same gas flow rate. Specifically, 1mm bubbles remove almost all of the inclusions larger than 30μm. However, it is unlikely that all of the bubbles that are this small could escape from the top surface. Those that are entrapped in the solidifying shell would generate serious defects in the steel product. Increasing bubble size above ~7mm produces no change in removal rate, likely due to the change in bubble shape offsetting the smaller number of bubbles.

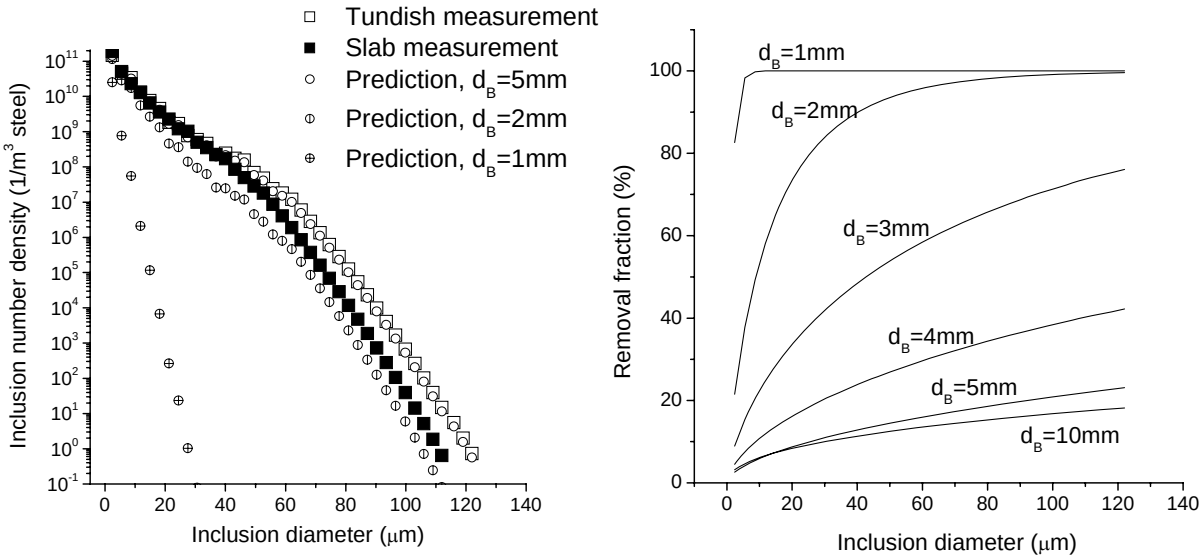

Fig. 4.2 Measured and calculated inclusion size distribution with different size bubble flotation (15 Nl/min gas)

As shown in Figure 4.3, increasing gas flow rate causes more inclusion removal by bubble flotation. Considering the effect of turbulent Stochastic motion slightly increases the inclusion removal by bubble flotation. For the current CC conditions, including a gas flow rate of 15 Nl/min, the bubble size is likely to be around 5mm, assuming there are a large number of active sites on the porous refractory that cause a gas flow rate of <0.5 ml/pore.[17] As shown in Figure 4.3, about 10% total oxygen is removed by bubble flotation. Previous work on this project indicate that ~8% of the small inclusions are removed to the top surface due to flow transport in the CC mold region.[47] Thus, the total predicted inclusion removal by flow transport and by bubble flotation is around 18%. The measured inclusion mass fraction is 66.8ppm in the tundish, and averages 51.9ppm in the slab, which corresponds to 22% removal in the mold (Fig.4.2). The prediction and the measurement agree remarkably well, considering that some inclusions are likely entrapped to the SEN walls to cause clogging.

Decreasing bubble size is shown in Figs.4.2 and 4.3 to be more efficient at removing inclusions. As discussed before, however, small bubbles, such as those < 1mm, may be trapped into solidifying shell while moving through the lower recirculation zone. Thus, there should be an optimum bubble size, which gives not only high inclusion removal efficiencies, but also low entrapment rates. The present results suggest an optimal range of perhaps 2-4mm.

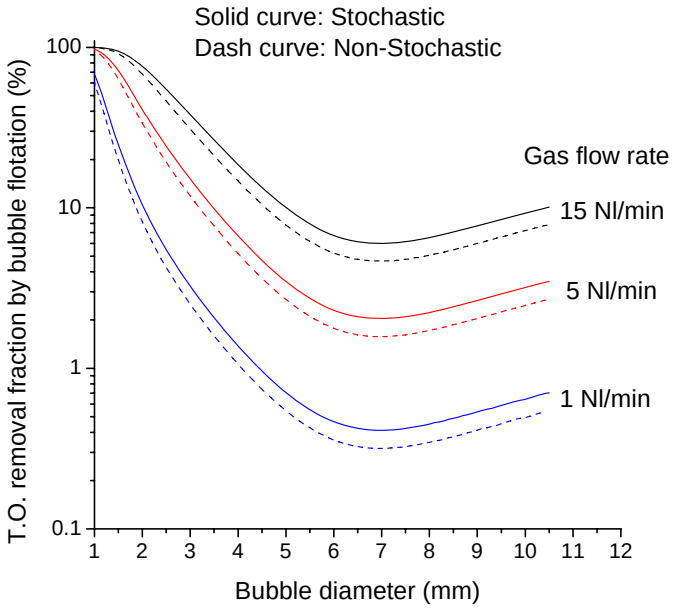

Fig. 4.3 Calculated inclusion removal by bubble flotation

4.4 Conclusions:

This work presents a fundamental model of inclusion removal due to bubble flotation in molten steel processing. The model is validated with available measurements and applied to predict the changes in inclusion distribution that occur in the mold region of a continuous slab caster. Specific model findings include:

- Smaller bubbles and larger inclusions have larger attachment probabilities. Bubbles smaller than 1mm diameter have inclusion attachment probabilities as high as 30%, while the inclusion attachment probability for bubbles larger than 5mm is less than 1%. The stochastic effect of turbulence (modeled by the random walk method) slightly increases the attachment rate.
- In the CC strand, smaller bubbles penetrate and circulate more deeply than larger ones. Bubbles larger than 1mm mainly move in the upper roll. 0.2mm bubbles can move as far as 6.65m and take 71.5s before they either escape from the top or are entrapped through the bottom, while 0.5mm bubbles move 3.34m and take 21.6s, 1mm bubbles move 1.67m and take 9.2s, and 5mm bubbles move 0.59m and take 0.6s.
- In the CC mold, if bubbles are ~ 5mm in diameter, ~10% of the inclusions are predicted to be removed by bubble flotation, corresponding to around 3ppm decrease in total oxygen. Combined with ~ 8% inclusion removal by flow transport, the total roughly agrees with the measured inclusion removal rate by the CC mold of ~22%.
- Smaller bubbles are more efficient at inclusion removal by bubble flotation, so long as they are not entrapped in the solidifying shell. Larger gas flow rate favors inclusion removal by bubble flotation. The optimum bubble size should be 2-4mm.

5 Flow and Heat Transfer in a Molten Flux Layer

Flux is added to the top of molten steel in the mold, where it melts to form a liquid slag or "flux" layer, which absorbs inclusions, and also acts as an insulator from heat loss through the top surface. This latter function is important to superheat transport and temperature near the meniscus, where hooks can trap inclusions if they are allowed to solidify.

The simulation results show that the Ra number for realistic liquid slag layers varies near the critical Ra number for the onset of natural convection. For fluxes with temperature-dependent viscosity, the variation of Nu with Ra is analogous to correlations for fluids with constant viscosity evaluated at the mean temperature, but the critical Ra number is larger, as shown in Fig. 5.1. The increase in Nu number with layer thickness is also quantified for realistic fluxes. For thin layers of realistic fluxes, natural convection is suppressed, so Nu increases linearly with increase of bottom shear velocity (Fig. 5.2). The increase is greater with decreasing average viscosity. The Nu increases nonlinearly with the increase of steel velocity due to the nonlinear relationship between steel velocity and flux bottom shear velocity (Fig. 5.3). The increase of heat transfer above pure conduction is only due to end effects, and hence depends on the dimensions of the layer. Larger increases observed in practice could be due to phenomena not included in these computations.

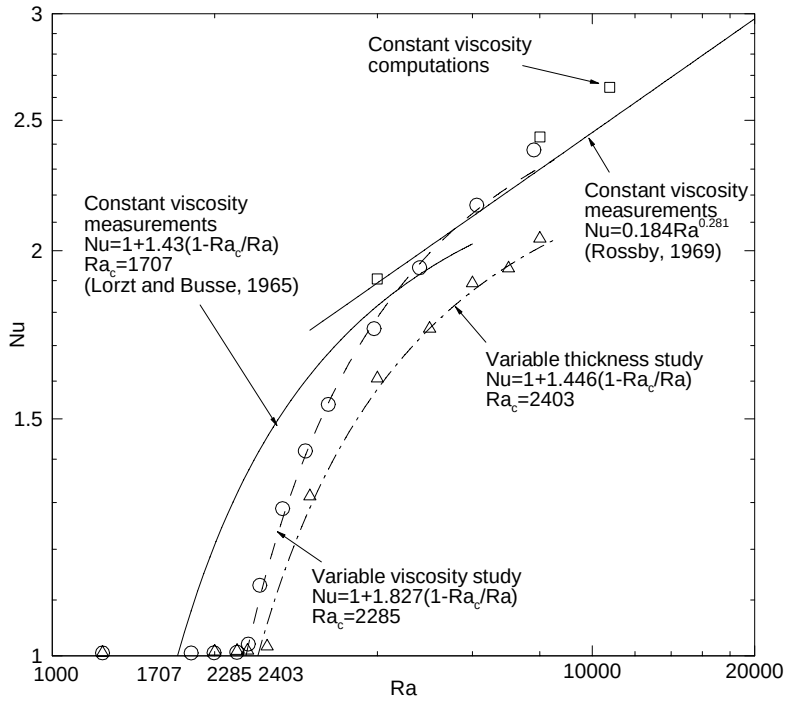

Fig. 5.1 Heat flow increase with convection strength (symbols are computed and lines are curve fits)

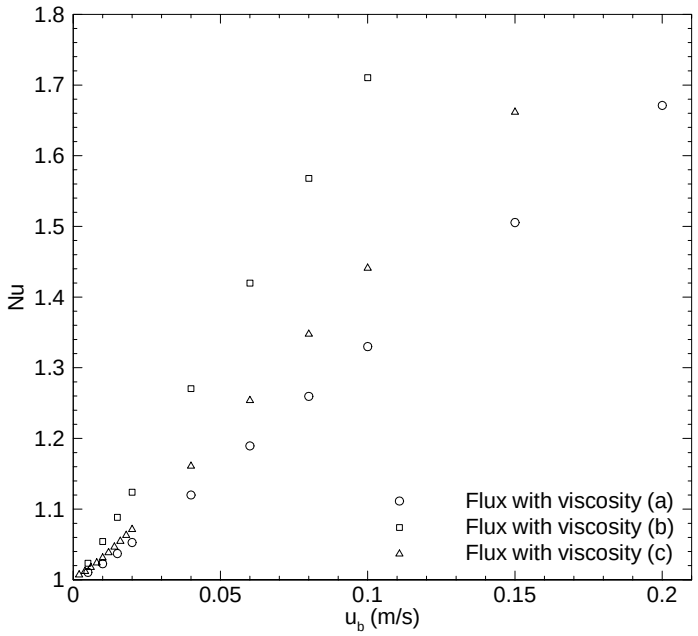

Fig. 5.2 Nu number as a function of bottom shear velocity

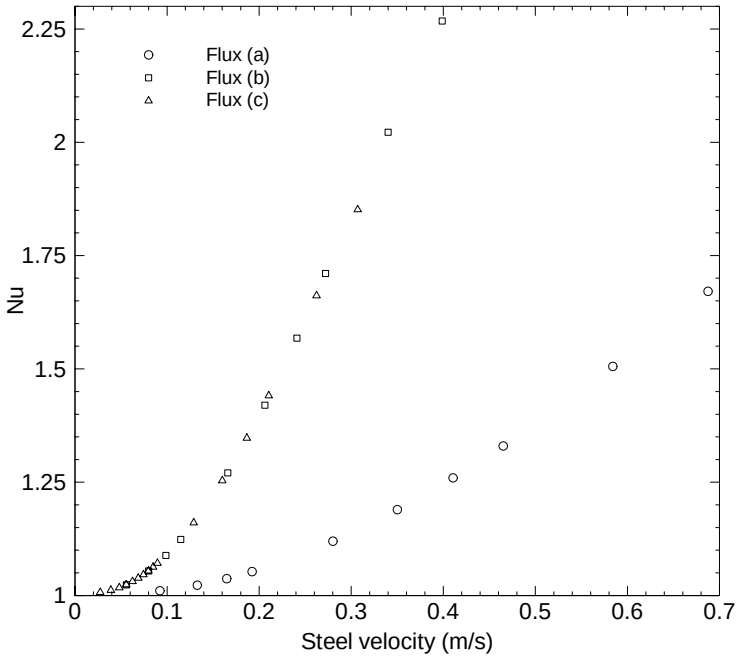

Fig. 5.3 Nu number as a function of steel velocity

6. Transient Flow and Super-Heat Transport in Continuous-Cast Steel Slabs

The flow in the liquid pool region features a steel jet coming out of the submerged nozzle entry and impinging obliquely on the narrow face in a confined space formed by the solidifying steel shell. The jet impingement causes locally high heat transfer rate to the shell. Quantifying the turbulent heat transfer to the shell during the critical early stages of solidification is of great importance to the understanding of phenomena in the casting process, meniscus hook formation, breakouts, internal structure of solidified steel, crack formation, etc. However, the high temperature environment of the process makes it very difficult for experimentation or direct measurement of the flow and temperature field. Scaled or full dimension water models can give some insight into the transient flow features of the process, but with its limitation, water models are unable to generate heat transfer results. Thus, the modeling of transient flow and heat transfer heavily relies on numerical methods. In this work, a 3-D large eddy simulation of mold region of a continuous steel caster was carried out to study the turbulent flow and heat transfer.

Average temperature field in the center plane is shown in Fig. 6.1. The jets have very hot cores at the pouring temperature, which diffuses quickly. Most of the jet is roughly 30K above the solidification temperature. Temperature in the upper roll region is quite uniform and has a superheat of about 20K. In the little recirculation at the top right corner, fluid is much cooler: only 5K over the freezing temperature. This is important to meniscus solidification. The coldest regions are near the solidifying shell and the between the wall jet and the center jet low in the domain, where the steel is cooled from both wide faces and there is no strong flow to carry in hotter steel. The important cold region at the meniscus at the corner of the top surface and the narrow face is caused by the little recirculation region at the corner. This recirculation region is thus detrimental and may cause serious quality problems due to hook formation and inclusion entrapment.[42]

The temperature profiles predicted in the upper roll region are compared with plant measurements in the same caster with the same casting condition. Figure 6.2 shows an example comparison of simulation results with the measurements. The temperature profile in the simulations match the experiment very well. This suggests that the temperature field and corresponding heat flux predictions are also accurate.

Figure 6.3 shows the average heat flux to the solidifying shell along the narrow face. The heat flux is the largest where the jet impinges on the narrow face. There is also a significant time variation, owing to chaotic fluctuations in the jet position. Elsewhere, there is a local heat flux maximum in the wide faces near the narrow face caused by the vortices generated by the impinging of the side jet. There are large regions of relatively high heat flux regions where the side jet, center jet and the wall jets touch the wide faces. In the narrow face, there is a little heat flux rise near the top surface, which is the result of the little recirculation region at the corner. The flow towards the SEN near the top surface creates relatively high heat flux region in the wide faces near the top surface. Also, the vortices generated as the flow towards SEN passes the SEN raise the heat flux to the wide faces above the center jet.

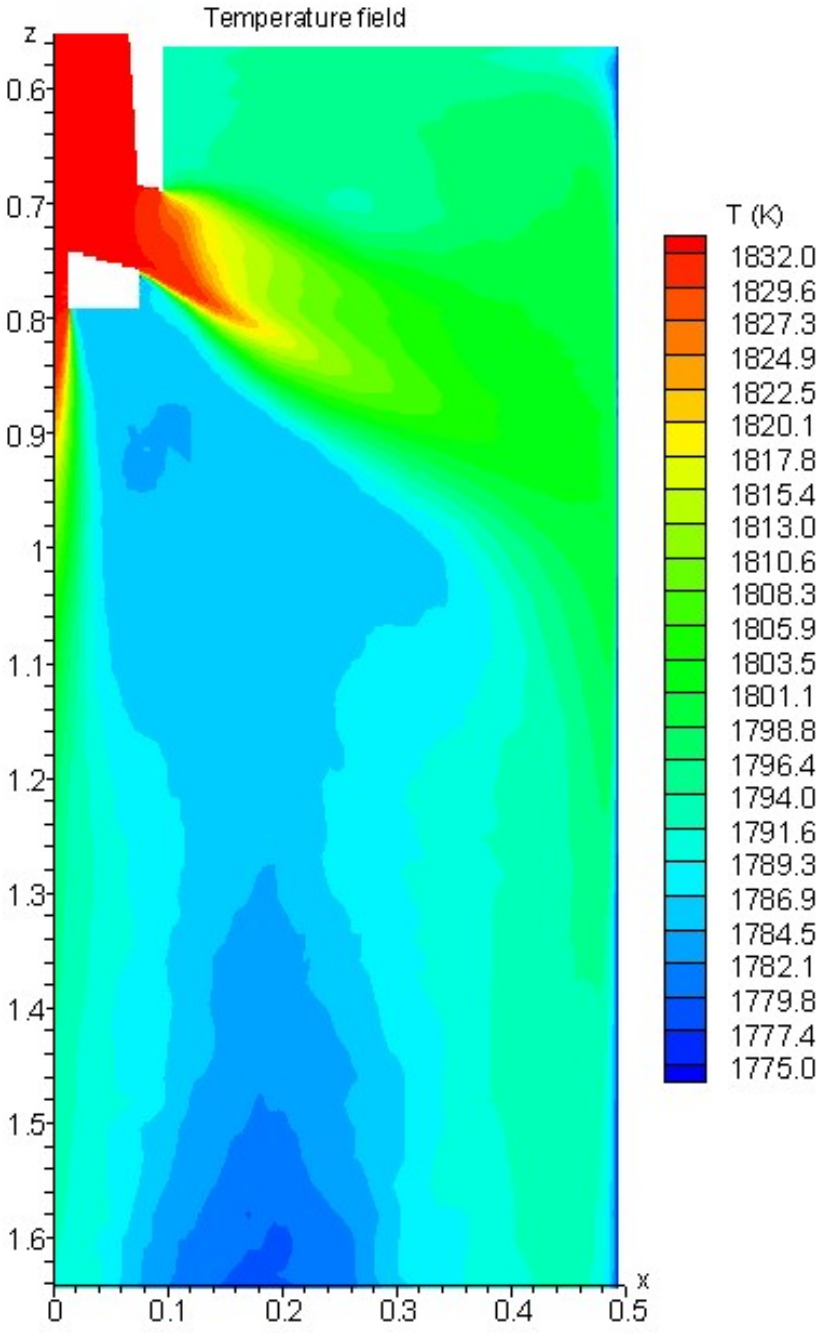

Fig. 6.1 Mean temperature field of center plane (with SGS model)

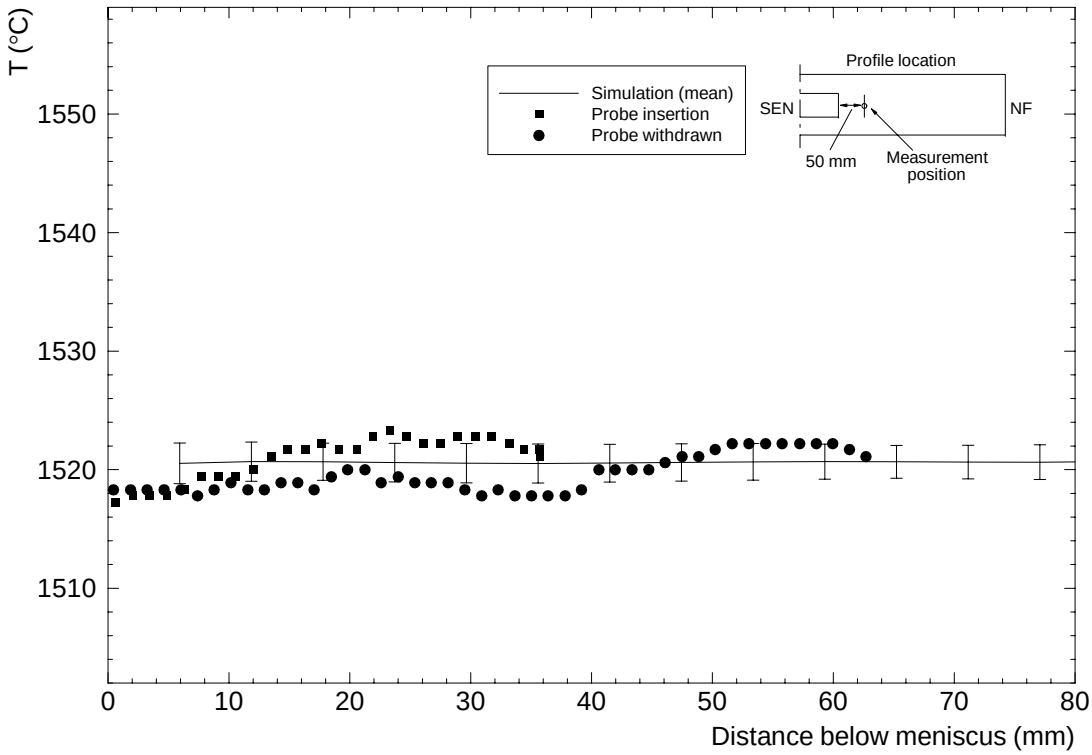

Fig. 6.2 Simulated and measured temperature profiles in molten steel (measurement 1, with SGS model)

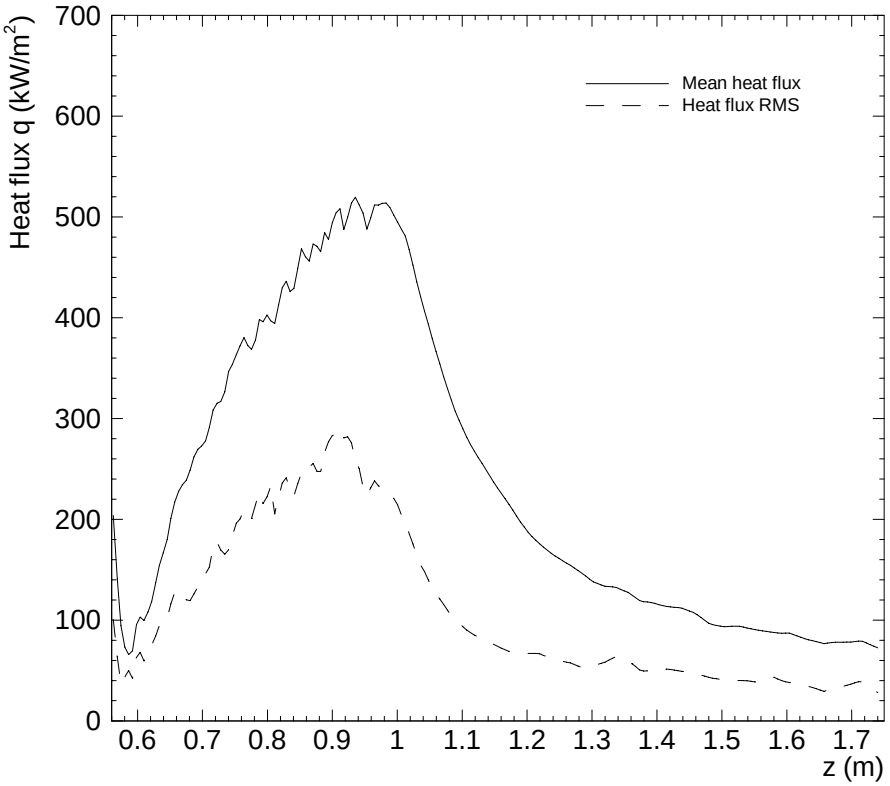

Fig. 6.3 Heat fluxes profile along narrow face centerline (with SGS model)

7. Interface Heat Transfer and Mold Friction

Findings from the models of heat transfer, mass and momentum balance of the flux layers, and friction at the interface between the steel shell and the oscillating mold wall include the following. Further details can be found elsewhere [61, 71].

1. Solid slag tends to remain attached to the mold wall, especially near the meniscus. When friction on the mold side cannot compensate the shear stress on the slag solid/liquid interface, axial stress builds up in the solid slag layer. If the powder consumption rate drops below a critical level, the axial stress can exceed the slag fracture strength, so the solid slag breaks and moves down the mold wall.
2. Crystalline slag with higher solidification temperature has a thick solid slag layer so lowers heat transfer across the mold/shell gap and increases shell surface temperature.
3. The slag temperature-viscosity curve determines the shear stress along the mold wall and affects both the critical consumption rate and possible slag fracture position. Crystalline slag (having a sharp viscosity transition) tends to fracture near the meniscus, but not easily (lower critical Q_{lub}). Glassy slag (having a gradual viscosity rise at lower temperature) tends to fracture near mold exit, easily (higher critical Q_{lub}). Increasing slag solidification temperature and decreasing hightemperature viscosity (such as occurs with high basicity slag) tends to lower critical Q_{lub} and make it less easy to fracture.
4. The following variables lower axial stress in the solid slag layer, critical Q_{lub}, and the likelihood of slag fracture. - Increasing friction coefficient helps by encouraging the solid slag to stay attached to the mold wall. - Smaller oscillation marks lower gap friction and lower the danger of slag fracture. - Decreasing casting speed lowers critical Q_{lub} and the danger of slag fracture at the meniscus, such as for slag A and for slag G cast at high speed. - Increasing casting speed is safer for avoiding slag fracture near mold exit, such as for slag G cast at low speed. - Increasing slag fracture strength helps slightly.
5. Liquid slag layer lubrication indicates a stable attached solid slag layer and can be recognized by very low mold shear stress (~1kPa) with a sinusoidal variation over each oscillation cycle.
6. The top half of the mold has negligible friction against the steel shell, as the liquid slag layer minimizes it. Solid slag friction begins just before the liquid slag runs out, lower down the mold. Increasing the fraction of the mold with solid slag friction can be identified by higher total mold friction and a sharper square wave shape of the friction curve over each cycle
7. The high friction (10~20kPa) measured in real casters might be due to any of three sources: an intermittent moving slag layer, excessive taper or mold misalignment. At low casting speed, the critical consumption rate is high, so variations in slag consumption at the meniscus can easily lead to solid slag layer fracture and movement. At high casting speed, excessive taper and mold misalignment likely increase friction problems.

Summary of Significant Findings

Advanced computational models have been developed to predict quantitatively, the removal of inclusions in the mold region during the continuous casting steel and related phenomena and processes. This multi-faceted research project includes the development and validation of models to predict transient fluid flow in the nozzle and mold, the transport of inclusion particles, the entrainment of particles from the top surface, the entrapment of inclusions by bubbles, the removal of particles to the top surface of the mold or their capture into the solidifying shell, and the optimization of fluid flow parameters to according to these findings. Each aspect of the models has been tested with plant measurements and applied to better understand and optimize the process to improve steel quality. Some of the significant findings from the seven subprojects include:

- Transient flow models require a fine mesh (400,000 nodes) to achieve accuracy within 17%.

- Model simulations of fluid flow can match measurements in both water models and steel casters, including liquid level variations of the top surface, calculated with a simplified model.

- At least 2500 particles are required to obtain statistics accurate within ±3% for inclusion transport in the mold. The initial removal rates are chaotic, and depend on time variations in the flow.

- Although the safe removal of inclusion particles to the top surface increases with increasing particle size, the removal fractions are still small: only ~12% of 100 μm particles or 70% of 400μm particles are removed. Only 8% of small particles (10μm and 40μm) are removed. Varying nozzle geometry, such as using a shallower port angle, can only improve removal slightly.

- The removal of slag particles entrained from the top surface depends greatly on the particle size. Most (>92%) of the 250μm - 400μm droplets simply return to the slag layer. However, more than half of the 100μm particles are eventually captured, leading to sliver defects.

- A short (9s) burst of inclusions entering the caster takes about 4 minutes to remove for the casting conditions assumed here. The captured particles concentrate mainly within a 2-m long section of slab. Using this information from together with sensors to detect when inclusion bursts occur would allow the contaminated steel to be isolated.

- Flow transport tends to concentrate entrapped inclusions within 10-20mm beneath the strand surface, especially at the corner and towards the narrow faces. Thus, it is appropriate to focus inspection and slab conditioning efforts on improving the surface.

- Particle entrapment on refractory walls is a significant inclusion removal mechanism in addition to being associated with nozzle clogging, sudden release, and other quality problems.

- An efficient size-grouping model has been developed to simulate collisions in order to better model inclusion size distribution evolution starting from nucleation to final product size. Nucleation occurs ~10^8 times faster than mixing in the ladle

- Mixing computations have established an accurate methodology for inclusion particle motion in ladle refining, and have revealed guidelines for efficient ladle operation.

- Argon bubbles can remove significant quantities of inclusions, especially if they are small and are not captured into the final product. In the CC mold, if bubbles are ~ 5mm in diameter, ~10% of the inclusions are predicted to be removed by bubble flotation, corresponding to around 3ppm decrease in total oxygen. Combined with ~ 8% inclusion removal by flow transport, the total roughly agrees with the measured inclusion removal rate in the mold of ~22%.

- Mold flow parameters should be optimized to minimize level fluctuations and to avoid the entrainment of slag from the top surface. Specific gas flow rates and nozzle geometries to accomplish this are suggested for a particular set of casting conditions.

- Inclusions should be removed upstream of the mold, as much as possible, in order to minimize inclusion-based defects in the final product.

- Correlations have been developed to predict surface heat removal through the top surface flux layer as a function of its thickness, properties, and the tangential molten steel velocity beneath it. Natural convection cells are unlikely for typical real fluxes, because the temperature dependency of the viscosity damps out the local recirculation. Natural convection is significant only at the corners of the layer. These results will be useful in further models of the crucial meniscus region, which governs inclusion entrapment at the meniscus and other surface quality problems.

- Methodologies to accurately predict superheat transport during flowing molten metal with jet impingement have been developed, validated with plant measurements and applied to real casters. This benchmark computation will be important for further model validation and parametric studies to lessen problems with excessive shell thinning at the impingement point, and excessive meniscus solidification (and the corresponding inclusion entrapment and other defects).

- Models of behavior of the interfacial gap have been developed. These models will be important for relating mold sensor measurements (such as friction) with surface defects (such as lubrication problems), and choosing mold flux and operating conditions in order to optimize mold operation to improve surface quality.

Further details can be found in the 47 technical publications that resulted from this work.

Acknowledgments

This project was supported by the National Science Foundation (Grant # DMI-01-15486) with matching funds from the Continuous Casting Consortium at the University of Illinois. . The work here was performed by many students, including Q. Yuan, B. Zhao, Jun Aoki, and P. Sulikowski, Research Scientist, Lifeng Zhang with the help of co-PI Pratap Vanka, which is gratefully acknowledged. Thanks are also extended to industry researchers Ron O'Malley, formerly at AK Steel, P. Dauby, formerly at LTV Steel, S. Yang of Panzhihua Steel, X. Wang, K. Cai, J. Li, and X. Wan of University of Science and Technology, Beijing, and others who helped to obtain samples and plant data. Finally, thanks are due to FLUENT, Inc., for providing the FLUENT code, to the National Center for Supercomputing Applications at the University of Illinois for computing time.

References

1. "Continuously Cast Steel Output, 1999," International Iron Steel Institute, Brussels, Belgium, www.worldsteel.org, 2000.
2. Herbertson, J., Q.L. He, P.J. Flint and R.B. Mahapatra, "Modelling of Metal Delivery to Continuous Casting Moulds," in Steelmaking Conf. Proc., Vol. 74, ISS, Warrendale, PA, (Washington, D.C.), 1991, 171-185.
3. Honeyands, T. and J. Herbertson, "Oscillations in Thin Slab Caster Mold Flows," 127th ISIJ Meeting), ISIJ, Tokyo, Japan, 1994.
4. Thomas, B.G., "Application of Mathematical Models to the Continuous Slab Casting Mold.," Iron & Steelmaker (ISS Trans.), Vol. 16 (12), 1989, 53-66.
5. Thomas, B.G., "Mathematical Modeling of the Continuous Slab Casting Mold, a State of the Art Review," in Mold Operation for Quality and Productivity, A. Cramb, ed. Iron and Steel Society, Warrendale, PA, 1991, 69-82.
6. Thomas, B.G. and F.M. Najjar, "Finite-Element Modeling of Turbulent Fluid Flow and Heat Transfer in Continuous Casting," Applied Mathematical Modeling, Vol. 15 (5), 1991, 226-243.
7. Huang, X., B.G. Thomas and F.M. Najjar, "Modeling Superheat Removal during Continuous Casting of Steel Slabs," Metall. Trans. B, Vol. 23B (6), 1992, 339-356.
8. Huang, X. and B.G. Thomas, "Modeling of Steel Grade Transition in Continuous Slab Casting Processes," Metall. Trans., Vol. 24B (2), 1993, 379-393.
9. Hershey, D.E., B.G. Thomas and F.M. Najjar, "Turbulent Flow through Bifurcated Nozzles," Int. J. Num. Meth. in Fluids, Vol. 17 (1), 1993, 23-47.
10. Thomas, B.G. and X. Huang, "Effect of Argon Gas on Fluid Flow in a Continuous Slab Casting Mold," in 76th Steelmaking Conf. Proc., Vol. 76, Iron and Steel Society, Warrendale, PA, (Dallas, TX), 1993, 273-289.
11. Thomas, B.G., X. Huang and R.C. Sussman, "Simulation of Argon Gas Flow Effects in a Continuous Slab Caster," Metall. Trans. B, Vol. 25B (4), 1994, 527-547.
12. Lawson, G.D., S.C. Sander, W.H. Emling, A. Moitra and B.G. Thomas, "Prevention of Shell Thinning Breakouts Associated with Widening Width Changes," in Steelmaking Conf. Proc., Vol. 77, ISS, Warrendale, PA, (Chicago, IL), 1994, 329-336.
13. Najjar, F.M., B.G. Thomas and D.E. Hershey, "Turbulent Flow Simulations in Bifurcated Nozzles: Effects of Design and Casting Operation," Metall. Trans. B, Vol. 26B (4), 1995, 749-765.

14. McDavid, R. and B.G. Thomas, "Flow and Thermal Behavior of the Top-Surface Flux/ Powder Layers in Continuous Casting Molds," Metall. Trans. B, Vol. 27B (4), 1996, 672-685.
15. Thomas, B.G., A. Denissov and H. Bai, "Behavior of Argon Bubbles during Continuous Casting of Steel," in Steelmaking Conf. Proc., Vol. 80, ISS, Warrendale, PA., (Chicago, IL), 1997, 375-384.
16. Thomas, B.G., R. O'Malley, T. Shi, Y. Meng, D. Creech and D. Stone, "Validation of Fluid Flow and Solidification Simulation of a Continuous Thin Slab Caster," in Modeling of Casting, Welding, and Advanced Solidification Processes, Vol. IX, Shaker Verlag GmbH, Aachen, Germany, (Aachen, Germany, August 20-25, 2000), 2000, 769-776.
17. Bai, H. and B.G. Thomas, "Bubble Formation during Horizontal Gas Injection into Downward Flowing Liquid," Metall. Mater. Trans. B, Vol. 32B (6), 2001, 1143-1159.
18. Bai, H. and B.G. Thomas, "Turbulent Flow of Liquid Steel and Argon Bubbles in Slide-Gate Tundish Nozzles, Part I, Model Development and Validation," Metall. Mater. Trans. B, Vol. 32B (2), 2001, 253-267.
19. Bai, H. and B.G. Thomas, "Turbulent Flow of Liquid Steel and Argon Bubbles in Slide-Gate Tundish Nozzles, Part II, Effect of Operation Conditions and Nozzle Design," Metall. Mater. Trans. B, Vol. 32B (2), 2001, 269-284.
20. Bai, H. and B.G. Thomas, "Effects of Clogging, Argon Injection and Continuous Casting Conditions on Flow and Air Aspiration in Submerged Entry Nozzles," Metall. Mater. Trans. B, Vol. 32B (4), 2001, 707-722.
21. Thomas, B.G. and H. Bai, "Tundish Nozzle Clogging – Application of Computational Models," in Steelmaking Conf. Proc., Vol. 18, Iron and Steel Society, Warrendale, PA, (Baltimore, MD), 2001, 895-912.
22. Thomas, B.G., "Modeling Study of Intermixing in Tundish and Strand during a Continuous-Casting Grade Transition," Iron and Steelmaker, Vol. 24 (12), 1997, 83-96.
23. Huang, X. and B.G. Thomas, "Modeling of Transient Flow Phenomena in Continuous Casting of Steel," Canadian Metall. Quart., Vol. 37 (304), 1998, 197-212.
24. Thomas, B.G., H. Bai, S. Sivaramakrishnan and S.P. Vanka, "Detailed Simulation of Flow in Continuous Casting of Steel Using K-ε, LES, and PIV," International Symposium on Cutting Edge of Computer Simulation of Solidification and Processes, I. Ohnaka, ed., (Osaka, Japan, Nov. 14-16, 1999), ISIJ, 1999, 113-128.
25. Thomas, B.G. and S.P. Vanka, "Study of Transient Flow Structures in the Continuous Casting of Steel," NSF Design & Manufacturing Grantees Conference, (Long Beach, CA), NSF, Washington, D.C., 1999.
26. Thomas, B.G. and S.P. Vanka, "Study of Transient Flow Structures in the Continuous Casting of Steel," NSF Design & Manufacturing Grantees Conference, (Vancouver, Canada), NSF, Washington, D.C., 2000, 14p.
27. Vanka, S.P. and B.G. Thomas, "Study of Transient Flow Structures in the Continuous Casting of Steel," NSF Design & Manufacturing Grantees Conference, (Jan. 7-10, Tampa, FL), NSF, Washington, D.C., 2001, 14p.
28. Sivaramakrishnan, S., H. Bai, B.G. Thomas, P. Vanka, P. Dauby and M. Assar, "Transient Flow Structures in Continuous Cast Steel," in Ironmaking Conference Proceedings, Vol. 59, ISS, Warrendale, PA, (Pittsburgh, PA, March 26-29, 2000), 2000, 541-557.

29. Sivaramakrishnan, S., B.G. Thomas and S.P. Vanka, "Large Eddy Simulation of Turbulent Flow in Continuous Casting of Steel," in Materials Processing in the Computer Age, Vol. 3, V. Voller and H. Henein, eds., TMS, Warrendale, PA, 2000, 189-198.
30. Thomas, B.G., "Modeling of the Continuous Casting of Steel: Past, Present, and Future, Dr. J. Keith Brimacombe Lecture," in Electric Furnace Conf. Proc., Vol. 59, ISS, Warrendale, PA, (Phoenix, AZ), 2001, 3-30.
31. Emling, W.H., T.A. Waugaman, S.L. Feldbauer and A.W. Cramb, "Subsurface Mold Slag Entrainment in Ultra-Low Carbon Steels," in Steelmaking Conf. Proc., Vol. 77, ISS, Warrendale, PA, (Chicago, IL), 1994, 371-379.
32. Sussman, R.C., M. Burns, X. Huang and B.G. Thomas, "Inclusion Particle Behavior in a Continuous Slab Casting Mold," in 10th Process Technology Conference Proc., Vol. 10, Iron and Steel Society, Warrendale, PA, (Toronto, Canada, April 5-8, 1992), 1992, 291-304.
33. Thomas, B.G., Q. Yuan, L. Zhang and S.P. Vanka, "Flow Dynamics and Inclusion Transport in Continuous Casting of Steel," 2003 NSF Design, Service, and Manufacturing Grantees and Research Conf. Proceedings, R.G. Reddy, ed., (Burmingham, AL, Jan. 6-9, 2003), University of Alabama, Tuscaloosa, AL 35498, 2003, 2328-2362.
34. Thomas, B.G., Q. Yuan, L. Zhang, B. Zhao and S.P. Vanka, "Flow Dynamics and Inclusion Transport in Continuous Casting of Steel," 2004 NSF Design, Service, and Manufacturing Grantees and Research Conf. Proceedings, (Dallas, TX, Jan. 5-8, 2004), Southern Methodist University, Dallas, TX, 2004, T/BGT/1-41.
35. Thomas, B.G., L. Zhang, Q. Yuan and S.P. Vanka, "Flow Dynamics and Inclusion Transport in Continuous Casting of Steel," 2005 NSF Design, Manufacture and Industrial Innovation Grantees Conf. Proceedings, J. Shaw, ed., (Scottsdale, AZ, Jan. 3-6, 2005), Arizona State Univ., Tempe, AZ, Vol. MPM #DMI0115486, 2005, T/BGT/1-24.
36. Thomas, B.G., R.J. O'Malley and D.T. Stone, "Measurement of temperature, solidification, and microstructure in a continuous cast thin slab," Modeling of Casting, Welding, and Advanced Solidification Processes, B.G. Thomas and C. Beckermann, eds., (San Diego, CA), TMS, Warrendale, PA, Vol. VIII, 1998, 1185-1199.
37. Yuan, Q., B. Zhao, S.P. Vanka and B.G. Thomas, "Study of Computational Issues in Simulation of Transient Flow in Continuous Casting," Materials Science & Technology 2004, (New Orleans, LA, Sept. 26-29), TMS, Warrendale, PA, Vol. II, 2004, 333-343.
38. Yuan, Q., B. Zhao, S.P. Vanka and B.G. Thomas, "Study of Computational Issues in Simulation of Transient Flow in Continuous Casting," Steel Research International, 2004, in press.
39. Yuan, Q., B.G. Thomas and S.P. Vanka, "Study of Transient Flow and Particle Transport during Continuous Casting of Steel Slabs, Part 1. Fluid Flow," Metall. & Materials Trans. B, submitted August, 2003.
40. Yuan, Q., "Modeling of Particle Engulfment / Pushing at Solidification Front during Continuous Casting of Steel," ME497 Final Report, University of Illinois at Urbana-Champaign, May 14, 2002.
41. Yuan, Q., B.G. Thomas and S.P. Vanka, "Study of Transient Flow and Particle Transport during Continuous Casting of Steel Slabs, Part 2. Particle Transport," Metall. & Materials Trans. B, accepted October, 2003.

42. Thomas, B.G., "Chapter 14. Fluid Flow in the Mold," in Making, Shaping and Treating of Steel: Continuous Casting, Vol. 5, A. Cramb, ed. AISE Steel Foundation, Pittsburgh, PA, 2003, 14.1-14.41.
43. Schade, J.H., R.J. O'Malley, F.L. Kemeny, Y. Sahai and D.J. Zacharias, "Chapter 13: Tundish Operations," in The Making, Shaping and Treating of Steel, 11th Edition, Casting Volume, A.W. Cramb, ed. The AISE Steel Foundation, (Pittsburgh, PA), 2003, 70.
44. Knoepke, J., M. Hubbard, J. Kelly, R. Kittridge and J. Lucas, "Pencil Blister Reduction at Inland Steel Company," in Steelmaking Conf. Proc., Vol. 77, ISS, Warrendale, PA, (Chicago, IL), 1994, 381-388.
45. Zhang, L. and B.G. Thomas, "State of the Art in Evaluation and Control of Steel Cleanliness," ISIJ International, Vol. 43 (3), 2003, 271-291.
46. Grimm, B., P. Andrzejewski, K. Muller and K.-H. Tacke, "Inclusions in Continuously Cast Steel Slabs-Numerical Model and Validation," Steel Res., Vol. 70 (10), 1999.
47. Zhang, L., B.G. Thomas, Kaike Cai, Jian Cui and L. Zhu, "Inclusion Investigation during Clean Steel Production at Baosteel," in ISSTech 2003 Steelmaking Conf. Proc., Vol. 86, ISS, Warrendale, PA, (Indianapolis, IN, Apr. 27-30, 2003), 2003, 141-156.
48. Wilde, G. and J.H. Perepezko, "Experimental Study of Particle Incorporation During Dendritic Solidification," Materials Science & Engineering A, Vol. 283, 2000, 25-37.
49. J-H.Jeong, N. Goldenfeld and J.A. Dantzig, "Phase Field Model for Three-Dimensional Dendritic Growth with Fluid Flow," Physical Review E, Vol. 64, 2001, 1-14.
50. Kurz, W. and D.F. Fisher, Fundamentals of Solidification, Trans Tech Publications SA, Aedermannsdorf, Switzerland, 1984, 242.
51. Shibata, H., H. Yin, S. Yoshinaga, T. Emi and M. Suzuki, "In-Situ Observation of Engulfment and Pushing of Nonmetallic Inclusions in Steel Melt by Advancing Melt/Solid Interface," ISIJ International, Vol. 38 (2), 1998, 149-156.
52. Stefanescu, D.M., F.R. Juretzko, B.K. Dhindaw, A. Catalina and S. Sen, "Particle Engulfment and Pushing by Solidifying Interfaces: Part II. Microgravity Experiments and Theoretical Analysis," Metallurgical and Materials Transactions A, Vol. 29A, 1998, 1697-1706.
53. Han, Q. and J.D. Hunt, "Particle Pushing: Critical Flow Rate Required to Put Particles into Motion," J. Crystal Growth, Vol. 152, 1995, 221-227.
54. Han, Q., "The Mechanisms for Particle Pushing," PhD Thesis, University of Oxford, Oxford, UK, 1994.
55. Yuan, Q., "Transient Study of Turbulent Flow and Particle Transport During Continuous Casting of Steel Slabs," PhD Thesis, University of Illinois at Urbana-Champaign, IL, 2004.
56. Yuan, Q., B.G. Thomas and S.P. Vanka, "Study of Transient Flow and Particle Transport during Continuous Casting of Steel Slabs, Part 1. Fluid Flow," Metal. & Material Trans. B., Vol. 35B (4), 2004, 685-702.
57. Gupta, D. and A.K. Lahiri, "A Water Model Study of the Flow Asymmetry Inside a Continuous Slab Casting Mold," Metall. Mater. Trans. B, Vol. 27B (5), 1996, 757-764.
58. Zhang, L., S. Yang, X. Wang, K. Cai, J. Li, X. Wan and B.G. Thomas, "Physical, Numerical and Industrial Investigation of Fluid Flow and Steel Cleanliness in the Continuous Casting Mold at Panzhihua Steel," in AISTech2004, ISS, Warrendale, PA, (Nashville, TN), 2004, 879-894.

59. Zhang, L., S. Yang, X. Wang, K. Cai, J. Li, X. Wan and B.G. Thomas, "Investigation of Fluid Flow and Steel Cleanliness in the Continuous Casting Strand," Metallurgical and Materials Transactions B (submitted June 13), 2005.
60. Nomura, O., "Influence of Continuous Casting Submerged Nozzle on Quality of Cast Steel," Seramikkusu (Ceramics Japan), Vol. 35 (8), 2000, 617-621.
61. Meng, Y. and B.G. Thomas, "Heat Transfer and Solidification Model of Continuous Slab Casting: CON1D," Metal. & Material Trans., Vol. 34B (5), 2003, 685-705.
62. Zhang, L., W. Pluschkell, and B.G. Thomas, "Nucleation and Growth of Alumina Inclusions During Steel Deoxidation," in Steelmaking Conf. Proc., Vol. 85, ISS, Warrendale, PA, (Nashville, March 10-13, 2002), 2002, 463-476.
63. Zhang, L. and B.G. Thomas, "Inclusion Nucleation, Growth, and Mixing during Steel Deoxidation," Continuous Casting Consortium Report, No. CCC200206, University of Illinois at Urbana-Champaign, 2003, 1-19.
64. Zhang, L. and B.G. Thomas, "Alumina Inclusion Behavior During Steel Deoxidation," 7th European Electric Steelmaking Conference, (May 26-29, 2002, Venice, Italy), Associazione Italiana di Metallurgia, Milano, Italy, Vol. 2, 2002, 2.77-2.86.
65. Nakanishi, K., J. Szekely, T. Fujii, Y. Mihara and S. Iwaoka, "Stirring and its Effect on Aluminum Deoxidation of Steel in the ASEA-SKF Furnace: Part I. Plant Scale Measurements and Preliminary Analysis," Metal. Trans. B., Vol. 6B (3), 1975, 111-118.
66. Oeters, F., Metallurgy of Steelmaking, Verlag Stahleisen mbH, 1994, 347.
67. Kawawa, T. and M. Ohkubo, "A Kinetics on Deoxidation of Steel," Trans. ISIJ, Vol. 8, 1968, 203-219.
68. Szekely, J., C.W. Chang and T. Lehner, "Flow Phenomena, Mixing and Mass Transfer in Argon-Stirred Ladles," Ironmaking & Steelmaking, Vol. 6, 1979, 285.
69. Ogawa, K., "Slag Refining for Production of Clean Steel," in Nishiyama Memorial Seminar, Vol. 143/144, Iron and Steel Institute of Japan, (ISS, Tokyo), 1992, 137-166.
70. Matsuno, M., Y. Kikuchi, M. Komatsu, M. Arai, K. Watanabe and H. Nakashima, "Development of New Deoxidation Technique for RH Degassers," I & Smaker, Vol. 20 (7), 1993, 35-38.
71. Meng, Y. and B.G. Thomas, "Interfacial Friction-Related Phenomena in Continuous Casting with Mold Slags," Metall. & Materials Trans. B, Vol. 34B (5), 2003, 707-725.